

Optical Studies of Antiferromagnetism in Chromium and Its Alloys

A. S. Barker, Jr., and J. A. Ditzenberger

Bell Telephone Laboratories, Inc., Murray Hill, New Jersey 07974

(Received 29 December 1969)

Absorption peaks are observed in the infrared spectra of chromium and of chromium alloys in the antiferromagnetic state. These peaks arise from the excitation of electrons across the antiferromagnetic energy gap. For the incommensurate state at low temperatures, the absorption maximum occurs at $5.1kT_N$. In the commensurate state, the gap is larger, and the absorption maximum is roughly independent of T_N . The breadth and temperature dependence of the absorption in pure chromium are explained on the basis of electron-phonon scattering. Resistivity measurements, optical-anisotropy data, and absorption spectra at several temperatures are presented and discussed.

I. INTRODUCTION

Chromium appears to be unique among metals, forming an itinerant electron antiferromagnetic state below the Néel temperature, $T_N = 312^\circ\text{K}$. The spatially oscillating electron-spin polarization has been extensively studied by neutron spectroscopy to obtain the amplitude, period, and spin direction.¹⁻³ The adjective "itinerant" is used because the spins which align below 312°K belong to the mobile conduction electrons which provide the electrical conductivity. There are several pieces of evidence for the itinerant nature of the antiferromagnetism.⁴ One of the proofs is provided by the observation that the antiferromagnetic spin-density wave (SDW) is purely longitudinal at low temperatures and its period is incommensurate with the lattice. Such a SDW can be contrasted with the SDW in certain rare-earth metals. In Tb, Dy, and Ho there is thought to be a fixed localized spin on each lattice site. The spin direction varies in a spiral pattern. While the pitch of the spiral is incommensurate, the spin at each site is constant unlike the case of the incommensurate longitudinal spin pattern in chromium.

Lomer first pointed out that in chromium the electron Fermi surface at Γ [(0, 0, 0) in reciprocal space see Fig. 1] and the hole surface at H [(1, 0, 0) in reciprocal space] have almost identical shapes thereby enhancing the density-of-state factor in any coupling interaction.⁵ More precisely, if the electron surface at Γ is shifted by the wave vector $\vec{Q} = (2\pi/a)(0.95, 0, 0)$ it fits or "nests" against the hole surface at H . This nesting of the Fermi surface appears to be very close or exact in chromium and is probably the main reason for the occurrence of the itinerant antiferromagnetism. The coupling of the surfaces is provided by the Coulomb attraction of the electrons and holes. The appearance of the new wave vector Q in the problem means that there is a new peri-

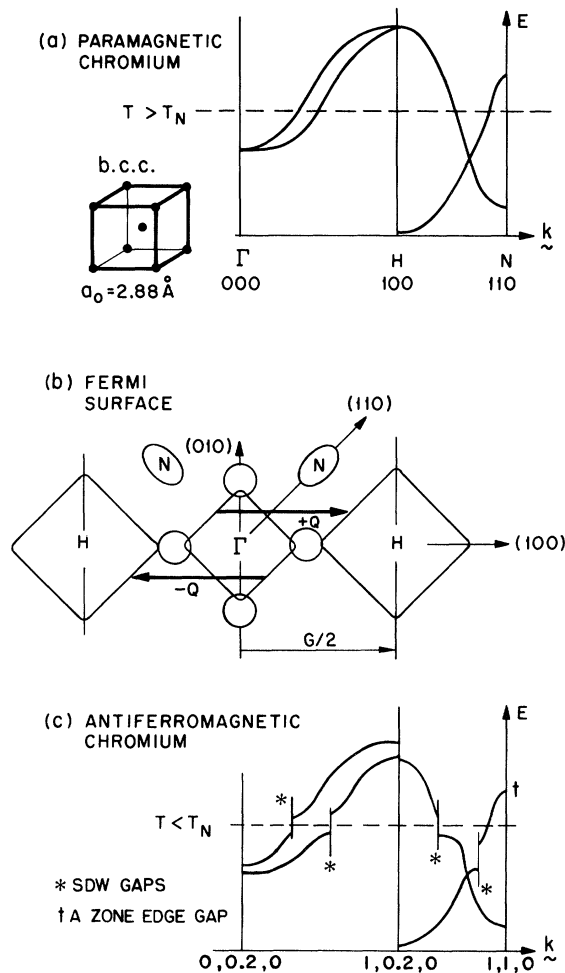


FIG. 1. (a) Unit cell and schematic band structure of chromium in the paramagnetic phase. The dashed line marks the Fermi level. (b) Fermi surface of paramagnetic chromium derived from the bands. Two Q vectors which cause nesting are shown. (c) New gaps in the band structure of antiferromagnetic chromium caused by the new periodicity associated with Q .

odicity in real space of $2\pi/Q = a/0.95$. In a simple bcc antiferromagnet, the new period would be $2\pi/Q = a$ in the [100] direction.

Overhauser has emphasized the spin-density wave properties of the interacting electrons in chromium and noted the mathematical similarity to the BCS theory of superconductivity.⁶ Fedders and Martin have carried out detailed calculations of a particular two-band model of chromium.⁷ These authors take the electron and hole portions of the Fermi surface to be spheres of equal radii and the attractive potential to be constant, independent of the wave vector. For such a model the nesting is perfect. Their results give a critical temperature T_N at which the system makes a second-order transition to a SDW ground state with wave vector Q . The periodicity of this wave causes gaps in the energy spectrum which are constant independent of wave vector because of their choice of a constant potential. It is an important result of the present work that the optical structure associated with the gap is fairly sharp, indicating that the energy gaps introduced in chromium are reasonably constant.

The SDW gaps are analogous to the zone-boundary gaps which already exist in the crystal due to the periodic-atomic potential. The zone-boundary gaps occur because of mixing of pairs of states separated by the reciprocal-lattice wave vector G . SDW gaps will occur for pairs of states separated by Q where Q is the separation of the electron and hole surfaces which couple. For the case of perfect nesting, every electron at the Fermi surface sees a hole state also at the Fermi surface displaced by Q so that even a very small gap caused by pairing will remove the entire electron and hole portions of the Fermi surface giving insulating behavior. In addition to the gaps described above, there will be coupling between states separated by $NQ \pm MG$. This coupling is weaker. The gaps here are called N th-order gaps. The second- and higher-order gaps are important for certain transport properties but are expected to be weak and to occur at very low frequency making the associated absorption very difficult to detect optically.

This paper is principally concerned with measuring the first-order SDW gaps by observing the corresponding optical transitions in the infrared spectral region. The optical transitions across a SDW gap are electric dipole allowed. This result at first seems contradictory for a SDW ground state. Detailed examination of the spin coupling shows that just below the gap the spin-up electrons are modulated by $\sin \vec{Q} \cdot \vec{r}$ and the spin-down wave functions by $\cos \vec{Q} \cdot \vec{r}$. Above the gap the modulation functions are reversed. Therefore, the elec-

tric dipole matrix element with no spin flip (i. e., absorption of a photon) is between $\sin \vec{Q} \cdot \vec{r}$ and $\cos \vec{Q} \cdot \vec{r}$ states which is allowed in first order. Figure 1 illustrates schematically the coupling and creation of a SDW gap. At the top of the figure some of the energy bands of chromium near the Fermi level for two principal directions are shown schematically.⁸ In Fig. 1(b) parts of the Fermi surface are shown. The principal electron and hole sheets at Γ and H are octahedral surfaces with rounded vertices. In addition there are electron "balls" on the points of the Γ sheet and hole ellipsoids at N .⁸ Next, a coupling of states linked by Q is considered. The Q of interest is that which causes "nesting," that is, a shift of Q brings most of the area of the electron surface at Γ into coincidence with most of the hole surface at H . Both $+\vec{Q}$ and $-\vec{Q}$ shown in Fig. 1 are equally effective and both occur simultaneously. Interactions cause the mixing of wave functions and the splitting of bands where they cross. Figure 1(c) shows the splittings and gaps formed for the bands illustrated. In chromium the distortions from perfect octahedral shape cause best matching to occur away from the octahedron points. The gaps probably open on the flat octahedral faces and are best seen by looking at energies along the line $(k, 0, 2, 0)$, for example, rather than along the line $(k, 0, 0)$. All gaps can be located by drawing the energy bands then redrawing the same bands shifted by $\pm \vec{Q} \pm N\vec{G}$. Points of intersection give the location of the SDW gaps.

There are several points to be made which can be visualized using Fig. 1.

(a) Because of the shapes of the pieces of Fermi surface, coupling of states displaced by $\pm \vec{Q}$ does not open gaps over the entire Fermi surface. The hole ellipsoids at N remain and parts of the hole surface at H probably remain. Chromium therefore retains some of its metallic properties below the transition temperature, though the electrical conductivity and electronic specific heat are reduced substantially.

(b) Best matching of Fermi surfaces occurs for $\pm \vec{Q}$ along 100, 010, or 001 axes. Detailed de Haas-van Alphen studies have shown that on cooling below T_N domains are formed.⁹ In any one domain there is one Q vector and the symmetry is reduced from cubic to tetragonal.⁹ Cooling the sample through T_N in a strong magnetic field H_0 favors the formation of a single domain through the entire crystal with $\pm \vec{Q}$ along the (100) axis closest to the direction of H_0 . Such a tetragonal crystal can be expected to show anisotropic optical properties. We expect the strongest gap absorption to show up for the infrared electric field polarized along $\pm \vec{Q}$.

(c) From Fig. 1 we note that if the Fermi level is raised (e.g., by alloying Cr with Mn to add electrons) the electron surface at Γ becomes larger and the hole surface at H smaller. More area will nest when the Γ surface is shifted by $\pm\vec{Q}$. If enough electrons are added, and the Fermi surfaces remain octahedral shaped, the sizes of the electron and hole surfaces will become equal so that $\vec{Q} = \frac{1}{2}\vec{G}$ which implies a commensurate antiferromagnetic state. Such commensurate-incommensurate transitions have been discussed theoretically.^{4, 10, 11} Rice has studied the effects of imperfect nesting using a model with spherical electron and hole Fermi surfaces of different radii.¹¹ He finds a first-order transition between the commensurate and incommensurate antiferromagnetic states as the difference in radii increases. It has been found that alloys of Cr do show this transition.¹²

As electrons are added \vec{Q} increases towards $\frac{1}{2}\vec{G}$, i.e., the factor 0.95 mentioned previously rises towards 1.000. T_N also increases indicating a more stable antiferromagnetic state. At a certain critical alloy concentration [near 0.3% Mn for the Cr (Mn) alloy] \vec{Q} jumps to $\frac{1}{2}\vec{G}$ discontinuously.¹² We find a discontinuous change in the optical absorption near this concentration also.

In Secs. II and III below, we discuss sample preparation and the infrared optical measurements. Section IV gives the results of the study of the energy gap for pure chromium as a function of temperature and crystal direction. Comparisons are made with the Fedders-Martin model as extended by Halperin and Rice to include electron-phonon coupling.¹³ In Sec. V the gap absorption

is discussed in both commensurate and incommensurate chromium alloys. Details of the magnitude of the anomalous skin effect and the actual optical constants of chromium are included in two Appendixes.

II. SAMPLE PREPARATION AND MEASUREMENTS

A. Sample Types

Table I shows the samples used in the present study. Four types of pure chromium were investigated. First "as-deposited" small single crystals about 2 mm \times 2 mm \times 10 mm purchased from Materials Research Corporation were examined. These had residual resistance ratios (RRR) of $\rho(300^\circ\text{K})/\rho(4.2^\circ\text{K}) \sim 800$. They exhibited the optical energy gap to be described below but were too small for many of the studies. Most of the spectra were taken on zone-refined single crystals obtained from Materials Research Corporation which had RRR ~ 200 . These crystals were 18 mm diam \times up to 30 mm long. Some of the single crystals were remelted to make a polycrystalline sample with crystallite size < 0.5 mm. This sample showed gap absorption also but with strength reduced about 25%. Finally a chromium film was evaporated onto polished sapphire in a vacuum of 10^{-6} Torr. It showed no gap nor even a resistive transition.

The chromium alloys were all formed by arc melting. Some samples as noted in Table I had molten zones passed through them in the arc furnace to give single crystals. The concentration of the minor constituent listed for each alloy is probably accurate to better than 10% of the concentration quoted. Figure 2 shows a section of the

TABLE I. Chromium samples.

Dopant element	Atomic percent	T_N ($^\circ\text{K}$)	T_{co}^a ($^\circ\text{K}$)	Comments and source
Pure	...	310	<i>I</i>	Single M. R. C. Corp.
Pure	...	310	<i>I</i>	Polycrystalline BTL
Pure	...	b	<i>I</i>	Evaporated film BTL
V	0.5	255	<i>I</i>	Single AMES
V	1.0	205	<i>I</i>	Single AMES
V	1.24	199	<i>I</i>	Polycrystalline BTL
Mo	5.0	~ 245	<i>I</i>	Single AMES
Mo	8.6	207	<i>I</i>	Polycrystalline BTL
Mn	1.0	451	60	Single AMES
Mn	1.76	~ 485	<i>C</i>	Single AMES
Ru	0.3	385	220	Polycrystalline BTL
Ru	0.65	460	70	Polycrystalline BTL
Ru	2.0	572	<i>C</i>	Polycrystalline BTL
Re	15.0	578	<i>C</i>	Polycrystalline BTL
Fe	3.0	?	254	Polycrystalline BTL

^aMost samples are either commensurate (*C*) or incommensurate (*I*) over the entire temperature range $0 < T < T_N$. For the remaining samples T_{co} is interpolated from data in Ref. 10.

^bNo transition detected in resistivity or optical spectra.

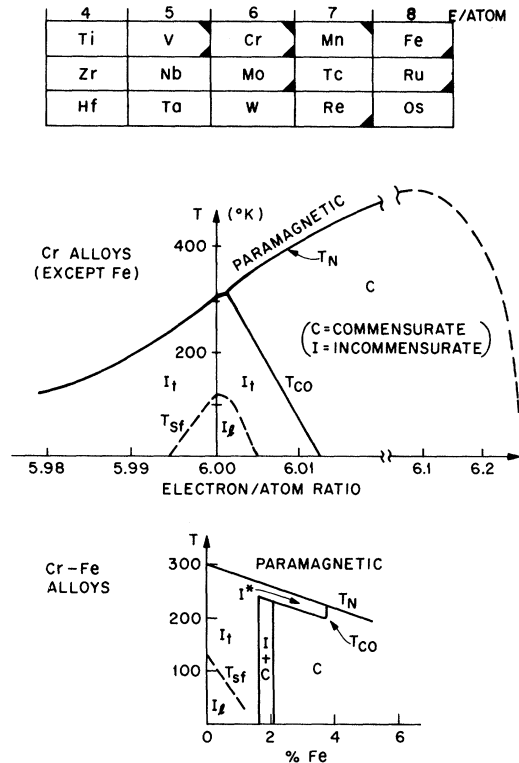


FIG. 2. Periodic Table near chromium and phase diagrams of chromium alloys. Shaded corners in table show alloys studied. Upper corner shading indicates single crystals were available, lower corner, polycrystals. The phase diagrams are schematic, particularly for Cr-Fe where some phases have not been firmly established. T_{∞} marks the commensurate-incommensurate phase boundary and T_{SF} marks the transverse (t)-longitudinal (l) SDW phase boundary.

atomic table near chromium. Chromium appears in column 6 (6 e /atom with atomic configuration $3d^54s$). Elements shown in partially shaded boxes have been used as diluents in chromium in the present optical studies. Upper corner shading indicates that single crystals were available. The remainder of Fig. 2 shows schematically the alloy phase diagram indicating the paramagnetic phase at high temperatures and the various antiferromagnetic phases at lower temperatures. Cr(Fe) alloys do not follow the general trends of the other alloy.^{14, 15} A separate diagram is given at the bottom of Fig. 2 for these alloys.

All samples were spark cut to expose a plane face about 8 mm \times 10 mm. This face was lapped using standard metallographic techniques. The sample was then electroetched in 5 parts perchloric acid to 100 parts glacial acetic acid. While the electroetch can destroy the flatness left by the mechanical lapping it was found absolutely essen-

tial for observation of the antiferromagnetic absorption to remove the surface damage caused by lapping.

B. Optical Configuration

Figure 3 shows the sample arrangement in the optical path. All three samples are carried on a holder which slides along the dashed line. The exit beam of a single-beam prism spectrometer is focused on the samples. By sliding the holder, samples 1 and 2 together or sample 3 alone reflects the beam. Sample 3 is always a front-surface aluminized mirror. In the early work samples 1 and 2 would be chromium samples cut from adjacent regions of the same crystal. The arrangement shown in Fig. 3 then measures the reflectivity cubed (R^3) when the intensity is measured relative to the aluminum mirror in position 3 and a correction is applied for the reflectivity of aluminum. Later an advantage was found in making sample 2 an aluminum mirror also. The ratio of the signals for the two configurations now gives R^2 (chromium) and needs no correction for R (aluminum). This advantage is important for low-temperature spectra since the change in aluminum reflectance with temperature is not well known.

As mentioned above, the electroetch process left the samples with a somewhat wavy surface. Since we require absolute reflectance for our

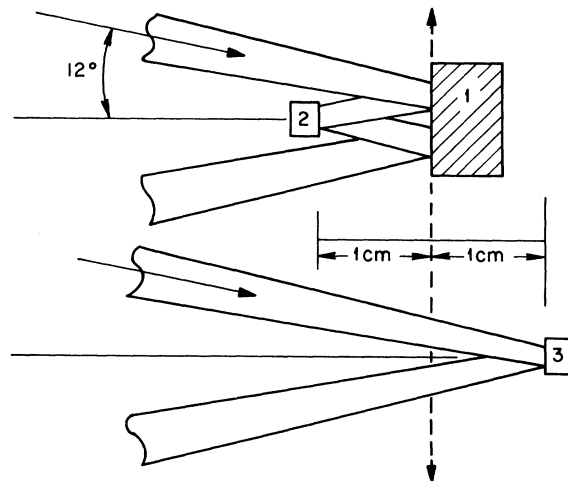


FIG. 3. Sample arrangement. All samples are mounted on a carriage which traverses along the dashed line to bring samples 1 and 2 or sample 3 into the beam. For convenience the infrared beam is shown for both sample positions simultaneously. Samples 2 and 3 are normally aluminum reference mirrors.

data analysis, each sample had a calibration run made at room temperature. For this run, aluminum was evaporated on half of the sample face. The reflectivity R^1 (chromium) was then measured with respect to this wavy aluminum mirror. This technique corrects for nonspecular reflection of the sample since both the sample and mirror now have similar wavy surfaces.

C. Resistivity Measurements

Bars for resistivity measurements were prepared for each sample. These were spark cut to about $2 \text{ mm} \times 2 \text{ mm} \times 12 \text{ mm}$ long. The long edges were then lapped into flatness and parallelism. Copper current and voltage leads were spot welded in place and a thermocouple cemented to the center of the bar. The resistivity (ρ) measurements were made on an x - y plotter (ρ versus T) for several cooling and heating runs. Precise measurements of ρ were made for some samples at fixed temperatures. The Néel temperature determined from the cusp in $\rho(T)$ is listed in Table I for each sample. The evaporated chromium film showed no resistivity anomaly.

III. DATA ANALYSIS

A. Reflectivity Measurements

Spectra of R^2 or R^3 were measured for the samples in the wavelength range $0.75\text{--}33 \mu$ ($300\text{--}13000 \text{ cm}^{-1}$) at various temperatures from 20 to 370°K . Using the method outlined in Sec. II the data were corrected for surface roughness and reduced to R . A Kramers-Kronig analysis was then performed to obtain the real and imaginary parts of the conductivity and other optical constants. Because of the range of data it is convenient to plot the absorptivity $A = 1 - R$ rather than R . Figure 4 shows a log-log plot of $1 - R$ for two aluminum films and the real part of the conductivity σ' obtained from the Kramers-Kronig analysis. The reflectivity data were obtained from the literature. We will use Fig. 4 to make several points. First we note that aluminum films prepared in ultrahigh vacuum (10^{-9} Torr) have higher reflectivities in the infrared.¹⁶ The corresponding infrared conductivity is somewhat lower. Typical values for aluminum films prepared in a moderate vacuum¹⁷ (such as our films) are shown also. These latter values of aluminum reflectivity were used where necessary in our data reduction to obtain the reflectivity of chromium.

B. Low-Frequency Region

At low frequencies ($\omega < 1/\tau$) we note from Fig. 2 that $1 - R$ tends towards a straight line with slope $\frac{1}{2}$. At 300°K , $1/\tau = 660 \text{ cm}^{-1}$ in aluminum.¹⁸ In

chromium, the present experiments and theoretical estimates put $1/\tau$ between 150 and 350 cm^{-1} at 300°K .¹³ Metals generally follow $1 - R \sim \omega^{1/2}$ at low frequencies. This is the Hagen-Rubens relation. The constant of proportionality is given in Table II. The antiferromagnetic absorption to be discussed below causes sharp structure in R near 1000 cm^{-1} . The Kramers-Kronig integral transform is somewhat local so that if we are interested in structure near 1000 cm^{-1} , the method used to extend R below 300 cm^{-1} is not very important. For the analysis of the chromium data we have extrapolated all spectra towards zero frequency using the Hagen-Rubens relation. Vertical double-ended arrows show the size of a $\pm 1\%$ uncertainty in R in Fig. 4. It is obvious that such a large uncertainty would not allow one to distinguish between the conductivity spectrum of our aluminum film and the ultrahigh-vacuum film. We have endeavored to work to $\pm 0.1\%$ in all measurements. The absolute R (chromium) may not be this accurate because of the correction for surface roughness and for R (aluminum). These corrections are smooth in frequency, however, so our analysis for sharp structure is reliable as has been borne out by various repeated analyses of samples for which several sets of data had been measured.

C. High-Frequency Region

Figure 4 shows that the aluminum reflectivity spectrum is fairly flat and featureless up to

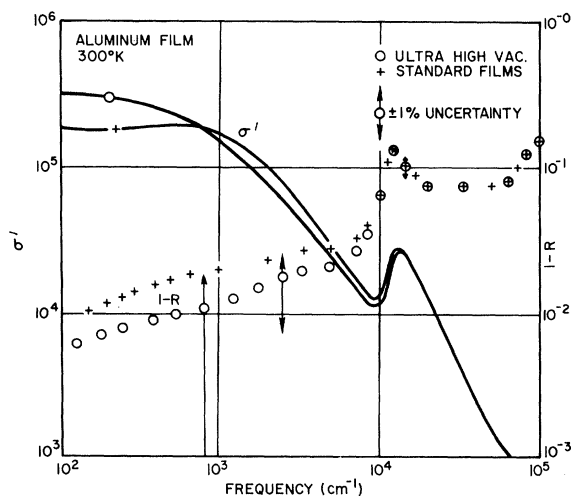


FIG. 4. Reflectivity spectra of two types of evaporated aluminum films. In this and succeeding figures we plot absorptivity $A = 1 - R$ for convenience. The solid curves show the conductivity spectrum obtained from R by Kramers-Kronig analysis.

TABLE II. Conductivity, dielectric function, and reflectivity for an electron-gas metal.

Drude conductivity	Dielectric function	
$\sigma \equiv i\omega\epsilon/4\pi = \sigma_0/(1 + i\omega\tau) - i\omega\epsilon_\infty/4\pi$	$\epsilon = \epsilon_\infty + \omega_n^2/(-\omega^2 + i\omega\omega_c)$ $= \epsilon_\infty - \frac{\omega_n^2 + i\omega_n^2\omega_c/\omega}{\omega^2 + \omega_c^2}$	
where: $\sigma_0 = ne^2\tau/m = ne^2l/mv_f$ $l = \text{mean free path}$ $v_f = \text{Fermi velocity} = l/\tau$	where: $\omega_n^2 = 4\pi ne^2/m$ $\omega_c = 1/\tau$ $\sigma_0 = \omega_n^2/4\pi\omega_c, \quad \sigma_0 = v_n^2/60\nu_c^a$	
f sum rule	Plasma frequency ($\epsilon = 0$)	
$\int_0^\infty \sigma' d\omega = \pi ne^2/2m = \frac{1}{8}\omega_n^2 = k_F^2 e^2/6\pi m$ $k_F = \text{Fermi wave vector}$	$\omega_p = \pm \omega_n/\epsilon_\infty^{1/2} (1 - \epsilon_\infty\omega_c^2/4\omega_n^2)^{1/2} + \frac{1}{2}i\omega_c$ $ \omega_p ^2 = \omega_n^2/\epsilon_\infty = 4\pi ne^2/m\epsilon_\infty$	
Hagens-Rubens region $\omega \ll \omega_c$	Reflectivity and absorptivity (a) Intermediate region $\omega_c < \omega < \omega_p$	
$A = 1 - R \approx 2(\nu/30\sigma_0)^{1/2}$	$A \approx 2(\nu_n/60\sigma_0)^{1/2}$ $A_0 \approx A + 3\nu_f/4c$ $A_1(\text{max}) \approx A(1 + 0.14x)^{1/2},^b$ for $x < 100$ $\approx A(0.04x)^{1/2},$ for $x > 100$ where: $x = 3l^2\omega_n^2/4c^2c^c$	classical skin effect anomalous skin effect diffuse surface scattering, $x > 1$ anomalous skin effect specular surface scattering

^aHere σ is in mho/cm and frequencies are in wave numbers $\nu(\text{cm}^{-1}) = \omega/2\pi c$.

^bThese are rough empirical formulas taken from Reuter and Sondheimer. A_1 is peaked at a frequency

given roughly by $\nu_c(1 + 0.4\sqrt{x})$.

^cThe x is a convenient dimensionless parameter. For $x \ll 1$ there is only classical skin effect.

10 000 cm^{-1} then shows a peak in $1 - R$. This peak is associated with excitations arising from an interband transition. The Kramers-Kronig analysis of the spectrum shows a corresponding peak in the real part of the conductivity, σ' . Pure chromium also has a peak in $1 - R$ near 15 000 cm^{-1} . We show in succeeding figures the conductivity peak associated with this structure for many of the samples. Accurate visible and ultraviolet spectra are not available for the chromium alloys. Our own rough measurements on some alloys show that they possess the same features as chromium with slightly shifted edges. Since most of the alloys are more than 95% chromium we expect no new features in the spectra in this region. Again, for the important antiferromagnetic structure near 1000 cm^{-1} , it is not critical how we extrapolate above 15 000 cm^{-1} . We have extrapolated to pure chromium data above this frequency for all samples.

D. Intermediate-Frequency Region

We now discuss the frequency region between $1/\tau$ and the plasma edge where the antiferromagnetic effects occur. Optical structure due to the

anomalous skin effect^{18,19} may also be present in this region and we discuss this effect first. Since the anomalous skin effect is extremely difficult to calculate we use a free-electron-gas model to estimate the size of the effect. The details of this analysis are given in Appendix A. In a metal the optical field has spatial Fourier components of wave vector $q \sim 1/\delta$ where δ is the skin depth. In the intermediate-frequency region δ becomes quite small, typically a few hundred angstroms. The optical field then has components with large q and selects conductivity components at finite q rather than at $q = 0$ as is assumed in the classical skin-effect regime. Figure 5 shows the wave vector and frequency-dependent conductivity for the free-electron model. From Fig. 5 we note that σ' at any finite q looks like a Drude function, i. e., like $\sigma'(q=0, \omega)$, but with increased collision frequency and decreased σ_0 . Considering classical skin-effect theory, such changes always reduce the reflectivity in the low- and intermediate-frequency regions (see Table II). Detailed consideration of the anomalous skin-effect theory for chromium (see Appendixes A and B) shows that there can be a reduction in R but of less than

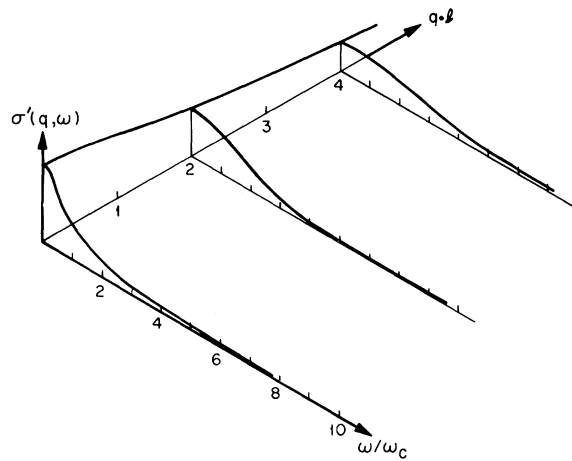


FIG. 5. Wave vector and frequency-dependent conductivity spectrum of an electron gas. For normal skin effect the conductivity along $q \cdot l = 0$ is sampled. In the anomalous-skin-effect regime conductivities at finite q become important in determining the reflectivity.

1%. This depressed reflectivity is not localized but occurs over at least a decade in frequency. By comparison the antiferromagnetic absorption is much more localized in frequency and generally causes a 3% dip in reflectivity. For these reasons we can use classical skin effect in all our data analysis. The limitations this procedure places on our accuracy in obtaining $\sigma'(\omega)$ are discussed in the Appendixes.

Figure 6 shows $1 - R$ for chromium and the real part of the conductivity obtained by the Kramers-Kronig analysis assuming classical skin effect as discussed above. Figure 7 and some of the succeeding figures show the spectra of pure chromium below the transition temperature and the spectra of several alloys analyzed in the same manner.

IV. RESULTS AND DISCUSSION: PURE CHROMIUM

A. Antiferromagnetic Part of Conductivity

Figures 6 and 7 show spectra of pure chromium at 300 and 80 °K. The major temperature-dependent features are a peak in σ' which appears near 1000 cm^{-1} and the reduction in σ' below 500 cm^{-1} . These two features appear together when the sample is cooled to 80 °K. These features are detectable at 200 °K, barely detectable at 273 °K but are undetectable in spectra taken at 300 and 373 °K (not shown). A small additional peak in σ' at 600 cm^{-1} reported earlier¹³ has been found to be a spurious instrumental response.

We wish now to isolate the antiferromagnetic part of the optical absorption, $\Delta\sigma'$. This proce-

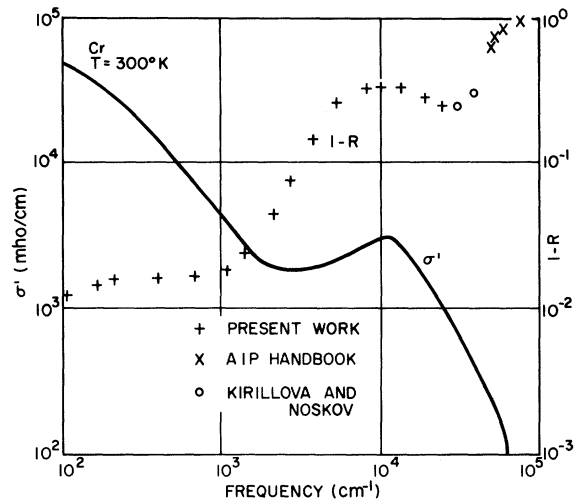


FIG. 6. Reflectivity spectrum of chromium at 300 °K. Since spectra at 320 °K showed no difference we regard this spectrum as typical of the paramagnetic phase. The solid curve shows the conductivity obtained by Kramers-Kronig analysis.

cedure is explained in some detail here and it applies to all the pure samples and alloys also. Appendix B discusses the actual form of the dispersion of the conductivity in pure chromium; here we wish only to isolate the antiferromagnetic part of σ with as few assumptions as possible. The problem can be visualized with a simple idealized model. If an energy gap opens up over part of the Fermi surface then free carriers which were participating in the intraband conduc-

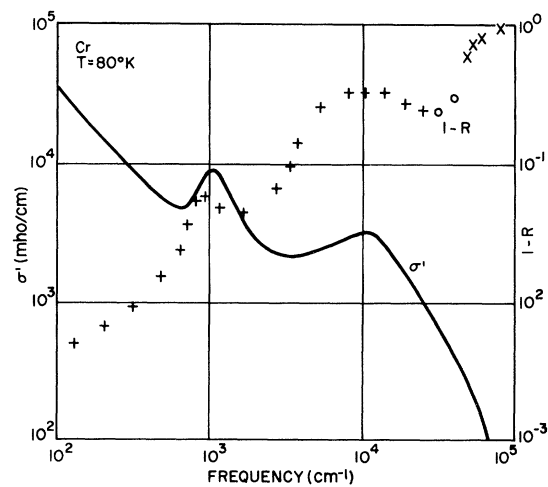


FIG. 7. Spectrum of antiferromagnetic chromium. Note the dip in R (peak in $1 - R$) at 1000 cm^{-1} . This dip produces the antiferromagnetic absorption peak seen in σ .

tion are frozen in on these parts and no longer contribute. For high enough photon energies they may again contribute by participating in transitions across the new gap that has appeared. There is, of course, a sum rule on the real part of the conductivity which ensures that new transitions must appear if we lose intraband conductivity. Figure 8 shows a highly idealized situation where the dc conductivity drops to half of its original value below T_N . The spectrum of σ' is taken to be of Drude form and τ is assumed not to change so that the entire spectrum falls to half its original height. The energy gap which caused the drop in σ' has width $\hbar\omega_g$ so that new transitions appear above ω_g . For the situation in Fig. 8(b), it is obvious how to isolate $\Delta\sigma'$. In this example σ' had Drude form below ω_g . This can be fitted to and extrapolated above ω_g and subtracted to leave the peak shown at the right-hand side of Fig. 8(b).

In real chromium, σ' is not of Drude form, thus it is difficult to separate out theoretically the free-carrier part. We proceed by assuming that at 300°K all absorption below 2500 cm^{-1} is free-carrier absorption. At 80°K we assume that the free-carrier part is just $\sigma'(300^\circ\text{K})$ times a constant scaling factor C . The antiferromagnetic part of the conductivity is calculated from

$$\Delta\sigma' = \sigma'(80^\circ\text{K}) - C\sigma'(300^\circ\text{K}). \quad (1)$$

Figure 9 shows the details of the subtraction and the resulting $\Delta\sigma'$ for $C=0.45$. In Fig. 9(b) $\Delta\sigma'$ is shown on a linear scale with uncertainty bars corresponding to our uncertainty in choosing C .

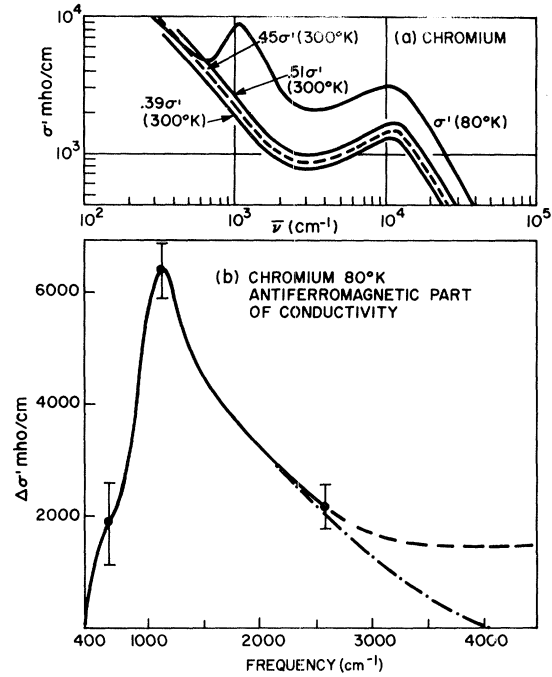


FIG. 9. Subtraction procedure for 80°K conductivity spectrum. Top of figure shows background (dashed) to be subtracted as well as uncertainty limits. Lower figure shows resultant antiferromagnetic part of conductivity. The dot-dashed extrapolation at high frequencies is thought to be the most realistic shape for $\Delta\sigma'$.

We have considered $C = 0.45 \pm 0.06$. This choice corresponds to making $\Delta\sigma'$ go to zero somewhere

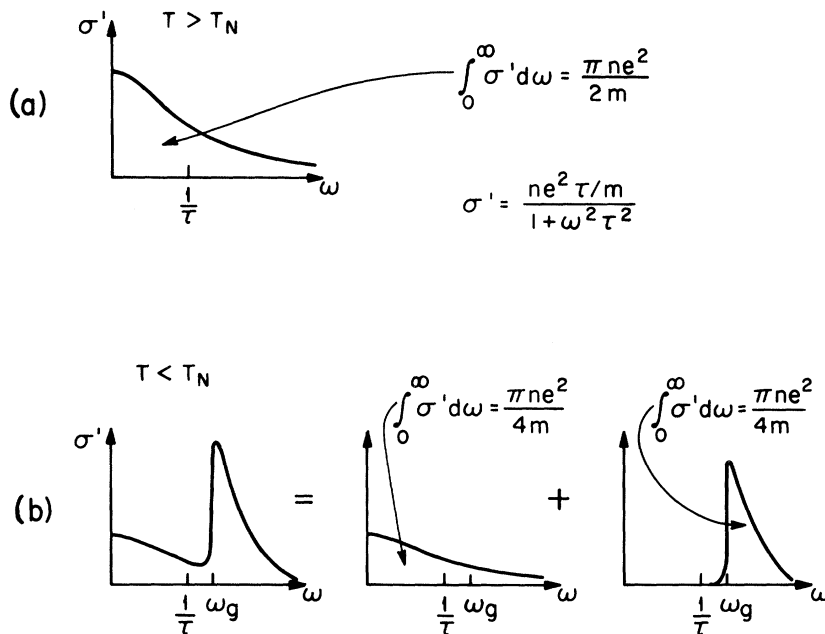


FIG. 8. Model spectra of a simple antiferromagnetic metal. (a) Paramagnetic conductivity spectrum has f -sum value of $\pi ne^2/2m$. (b) Antiferromagnetic spectrum has peak at the energy gap which accounts for half of the f sum in this example. The scattering time is assumed not to change on cooling through T_N .

in the frequency range 350 to 600 cm^{-1} . We emphasize that while the area under $\Delta\sigma'$ [Fig. 9(b)] is sensitive to the subtraction procedure, the absorption peak frequency is not. For most spectra the uncertainty in the frequency of the peak in $\Delta\sigma'$ is less than 5%.

For frequencies above 2500 cm^{-1} , the conductivity at all temperatures is dominated by an interband contribution which is peaked near 15 000 cm^{-1} . Obviously in this region the subtraction procedure is invalid. These high-energy transitions come from regions of the energy bands which are unaffected by the energy gap. The dot-dashed line in Fig. 9(b) indicates a reasonable extrapolation to correct the subtraction procedure at these high energies.

B. Energy Gap

Figure 9(b) shows the experimentally determined conductivity (absorption) associated with excitation across the SDW energy gap. Fedders and Martin have carried through calculations for perfectly nesting spherical electron and hole bands.⁷ They obtain a BCS-type integral equation for the antiferromagnetic state. In this model the energy gap $2\Delta_0$ at zero temperature is related to the transition temperature by the BCS relation

$$2\Delta_0 = 3.5 kT_N \quad (2)$$

The conductivity spectrum is

$$\Delta\sigma' = \frac{4e^2 k_F^3 \Delta^2 \tanh(\hbar\omega/4kT)}{3\pi m \hbar \omega^2 [(\hbar\omega)^2 - (2\Delta)^2]^{1/2}} \quad (3)$$

for $|\hbar\omega| > (2\Delta)$. k_F is the radius of the electron and hole Fermi spheres. At very low temperature Eq. (3) simplifies to

$$\Delta\sigma' \sim 1/\omega^2 [(\hbar\omega)^2 - (2\Delta)^2]^{1/2}, \quad |\hbar\omega| > 2\Delta_0 \quad (4)$$

Equation (4) contains a density-of-state factor familiar in superconductivity times an ω^{-3} factor which arises from evaluating the momentum matrix element between states above and below the gap (ω^{-2}) and converting this matrix element to conductivity (ω^{-1}).

The Fedders-Martin model has a threshold and infinite peak in $\Delta\sigma'$ at $\hbar\omega = 2\Delta$ at all temperatures. With increasing temperature the gap absorption threshold remains sharp and decreases in energy, disappearing at a second-order transition at T_N . The functional form is shown by a dashed curve in Fig. 10. Figure 10 also shows the measured absorption peaks at several temperatures. The BCS curve obviously lies too low. The theory also fails to explain the width and rounding of the observed absorption peak. Figure 11 shows the observed antiferromagnetic absorption at $T = 200$

$^\circ\text{K}$. The peak has moved lower in energy, and shows more rounding than the 80 $^\circ\text{K}$ data. The area under the curve is also reduced. There is relatively more uncertainty here in determining the area since the structure is less sharp and has moved lower in frequency where the free-carrier background is larger. The position of the absorption peak remains quite well defined, however, as indicated by the uncertainty bars in Fig. 10.

C. Absorption Strength and Sum Rule

Figure 12 shows the dc resistivity of a single-crystal sample of chromium. This sample was cooled without a magnetic field so that a single antiferromagnetic spin-density wave (single Q state) is not obtained. Arko, Marcus, and Reed have studied the resistivity for samples in a single Q state.²⁰ The results shown in Fig. 12 for a random collection of domains may be more appropriate for comparison with our optical data since, except for one or two runs, no attempt was made to obtain a single Q -state sample. Figure 10 shows that the resistance rises as the sample is cooled through the transition. This rise is associated with the freezing out of some carriers on the Fermi surface and (perhaps) with a change in the scattering lifetime of the remaining free carriers. Further cooling gives a net drop in resistivity because of the decrease in phonon scattering. McWhan and Rice have been able to measure the fractional increase in resistivity at low temperatures by suppressing the transition under high pressure.²¹ Their results (Fig. 12) suggest that $\Delta\rho/\rho$ approaches 0.3 at low temperatures. We wish now to compare this figure of 0.3

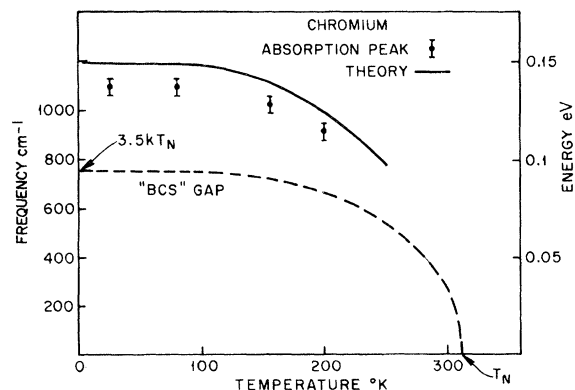


FIG. 10. Frequency of antiferromagnetic absorption peak as function of temperature. The points show the experimental results. For temperatures above 200 $^\circ\text{K}$ a peak is no longer discernable. The solid curve is the theoretical calculation which includes electron-phonon scattering.

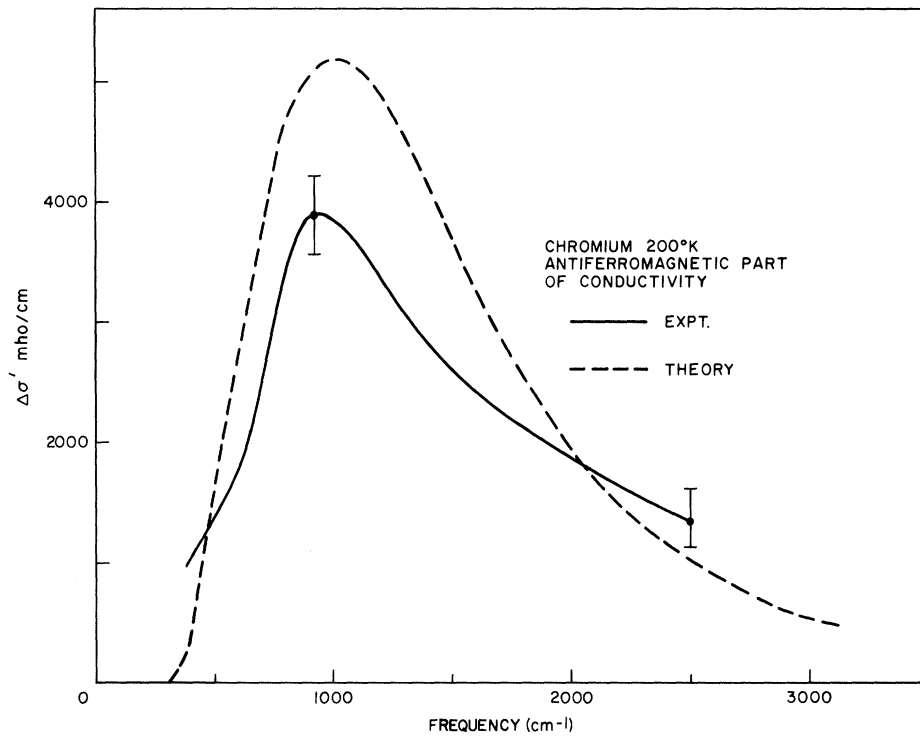


FIG. 11. Antiferromagnetic part of conductivity of chromium at 200°K.

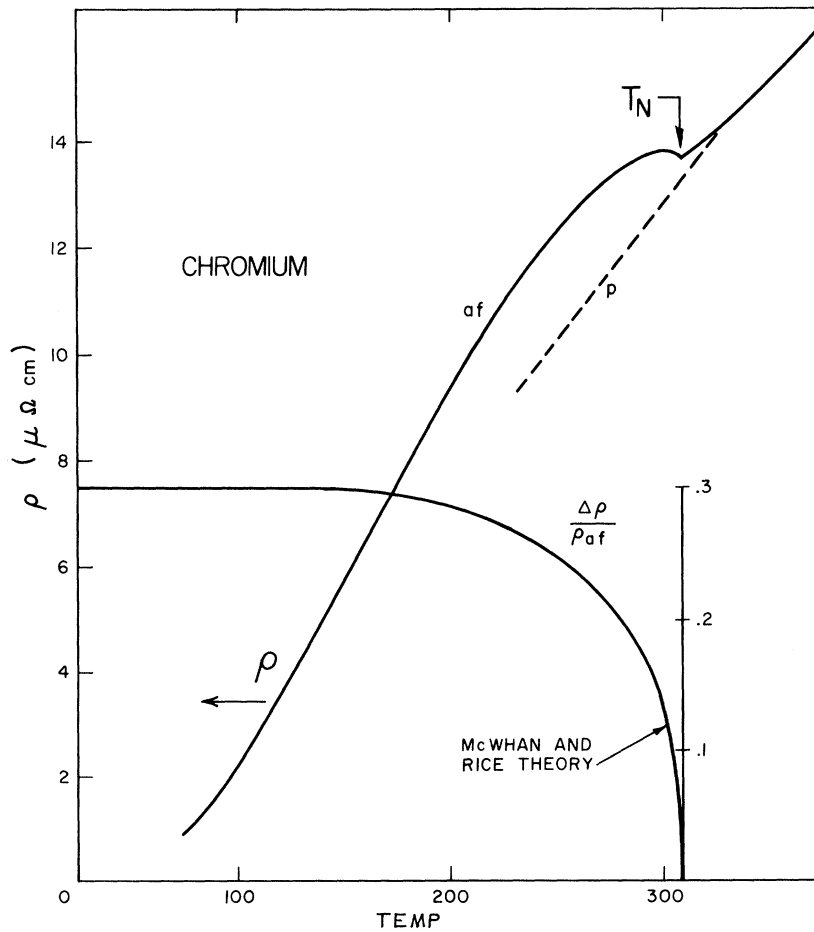


FIG. 12. Resistivity of chromium. The insert shows the theoretical value of the extra (antiferromagnetic) resistivity. The dashed line shows the paramagnetic resistivity which has been measured by McWhan and Rice by suppressing the transition using pressure.

with the integrated optical absorption using the sum rule. Table III shows the integrated conductivity from dc to 2000 cm^{-1} (where free carriers become less important than interband transitions). The f -sum value (A in Table III) suffers from quite large uncertainty because although we know $\sigma'(\omega=0)$ there are no measurements of σ' for $0 < \omega < 300 \text{ cm}^{-1}$. The uncertainty quoted was determined by assuming various reasonable shapes for σ' in this region. Table III shows that the integrated conductivity in the antiferromagnetic peak at low temperatures is about $\frac{1}{3}$ of the total integrated σ' . We conclude therefore that about $\frac{1}{3}$ of the carriers ($\frac{1}{3}$ of the Fermi surface) is involved in the formation of the gap. This figure is to be compared with 0.3 from the work of McWhan and Rice²¹ and 0.5 from measurements of the electronic specific heat.²² Table III shows that the integrated absorption in the antiferromagnetic peak falls somewhat at 200°K . Runs at 20°K are essentially the same as at 80°K so that the 80°K data can for most purposes be regarded as describing the $T=0$ case.

In Table III we also show the total value for the sum rule assuming $6 e/\text{atom}$. This value is 35 times larger than our free-carrier term A , i. e., we have accounted for only about $\frac{1}{6}$ of a carrier per atom in integrating our data from 0 to 2000 cm^{-1} . While we would not expect to attain the total f -sum value the result is surprisingly low. We can make two comparisons here. In aluminum we expect $3 e/\text{atom}$. The energy bands in aluminum are quite free-electron-like over most of the Fermi surface. It is found integrating the conductivity over only the Drude part gives $2.1 e/\text{atom}$.¹⁶ The total conductivity includes an

interband part beginning near 1 eV . On integrating the total conductivity, it is found that the sum rule begins saturating at $2.6 e/\text{atom}$ above 10 eV . Thus, for this free-electron-like metal integrating σ even up to 10 eV does not give the expected sum-rule value.

A second and perhaps better comparison can be made with tungsten. Here we have d bands similar to those we expect in chromium. Juenker *et al.* have evaluated the interband sum rule in the range $1\text{--}25 \text{ eV}$ ($8000\text{--}200\,000 \text{ cm}^{-1}$) for tungsten.²³ They find that the integral rises due to three broad conductivity peaks near 5 , 12 , and 17 eV accumulating an integrated value of roughly $6 e/\text{atom}$ in this range. Taking the known dc conductivity, assuming a Drude form, and estimating $\omega_c = 250 \text{ cm}^{-1}$ we obtain theoretically $\int_{\text{Drude}} \sigma d\omega \approx 0.5 e/\text{atom}$. Thus, most of the sum-rule contribution comes not from the low-frequency Drude region but from the energy region well above the collision frequency. In passing from tungsten to chromium, the d bands become narrower and the wave functions more localized so that the behavior is even farther removed from the free-electron model. Of course, the closer the approach to flat narrow bands, the larger the effective mass leading to a smaller f -sum contribution from the intraband conductivity. It is apparent from these comparisons that the d bands of chromium cause considerable shift of the weight in the f sum to energies well above the 4-eV limit of our spectra.

D. Theory Including Electron-Phonon Coupling

A complete theory of the occurrence of antiferromagnetism in chromium must involve the band structure and the wave-vector-dependent inter-

TABLE III. Conductivity sum rules.

Experimental	
Total "free-carrier" conductivity $T = 300^\circ\text{K}$	$A = \int_0^{2000} \sigma' d\nu = 34 \times 10^6 \text{ (mho/cm) cm}^{-1} \pm 15\%$
Antiferromagnetic absorption peak $T = 80^\circ\text{K}$	$B = \int_{400}^{4000} \Delta\sigma' d\nu = 9.7 \times 10^6 \text{ (mho/cm) cm}^{-1} \pm 15\%$
$T = 200^\circ\text{K}$	$C = \int_{400}^{4000} \Delta\sigma' d\nu = 5.0 \times 10^6 \text{ (mho/cm) cm}^{-1} \pm 15\%$
Fraction involved in gap formation $T = 80^\circ\text{K} = \frac{B}{A} = 0.28^{+0.10}_{-0.07}$	
f sum over entire experimental range (data in Table V) $T = 300^\circ\text{K}$	$\int_0^{30000} \sigma' d\nu = 1.8 \times 10^8 \text{ (mho/cm) cm}^{-1}$
Theoretical	
$n = 0.083 \times 10^{24} \text{ atom/cm}^3 \times 6 e/\text{atom} = 0.5 \times 10^{24} e/\text{cm}^3$	
$\int_0^\infty \sigma' d\nu = \pi n e^2 / 2m = 11.7 \times 10^8 \text{ (mho/cm) cm}^{-1} = 2.0 \times 10^{32} \text{ sec}^{-2} (\text{esu})$	

action between the carriers. The Fedders-Martin model based on a wave-vector-independent interaction and perfectly nesting Fermi spheres leads to the BCS value $\hbar\omega_p/kT_N = 3.5$ and an infinite peak in the conductivity [Eq. (3)]. The conductivity peak in chromium will be rounded by variations of the magnitude of the gap over the Fermi surface. Such variations are controlled by the wave-vector dependence of the interaction, and are therefore difficult to estimate theoretically. It is expected, however, that they will be small.

In addition the bands in chromium do not exhibit perfect nesting which will cause a renormalization of the ratio $\hbar\omega_p/kT_N$ away from 3.5. Kimball and Falicov,²⁴ Liu,²⁵ and Rice¹¹ have studied the renormalization of this ratio for various model band structures. They obtain values which depend on the model parameters but which are generally greater than 3.5. A third effect which rounds the conductivity peak and renormalizes $\hbar\omega_p/kT_N$ is electron-phonon scattering. Halperin and Rice have considered the effects of phonon scattering on the Fedders-Martin model.^{13, 26} Physically, we can picture the phonon scattering as smearing the Fermi surface and causing random electric fields in the lattice. Since the antiferromagnetic state is stabilized by the attraction of electron-hole pairs, the electron

phonon interaction provides a depairing mechanism. Using an estimate of the electron-phonon coupling parameter appropriate to chromium, Halperin and Rice find a broadening of the optical absorption and a renormalization of $\hbar\omega_p/kT_N$ from 3.5 to 5.2. We make some comparisons with this theory realizing, however, that band-structure effects which are neglected may also be important and certainly must be incorporated to understand the optical data of the commensurate chromium alloys.

Figure 13 shows the antiferromagnetic absorption calculated at $T=0$ using the phonon coupling theory of Halperin and Rice.^{13, 26} The theory has one free parameter which is chosen to give the theoretical curve the same integrated area as the experimental curve. The agreement is very pleasing both as to peak position and peak shape. Once the scaling parameter has been fixed, calculations of $\Delta\sigma$ (theory) can be carried out at other temperatures. The dashed curve in Fig. 11 shows a calculation at $T=200^\circ\text{K}$. Experimentally, the peak (solid curve Fig. 11) has shifted to lower energy, has developed a more rounded top, and has lost about half of its area compared with the 300°K peak. The theoretical curve with no adjustable parameters gives very reasonable agreement for the shift and rounding but predicts only a 12% decrease in area.

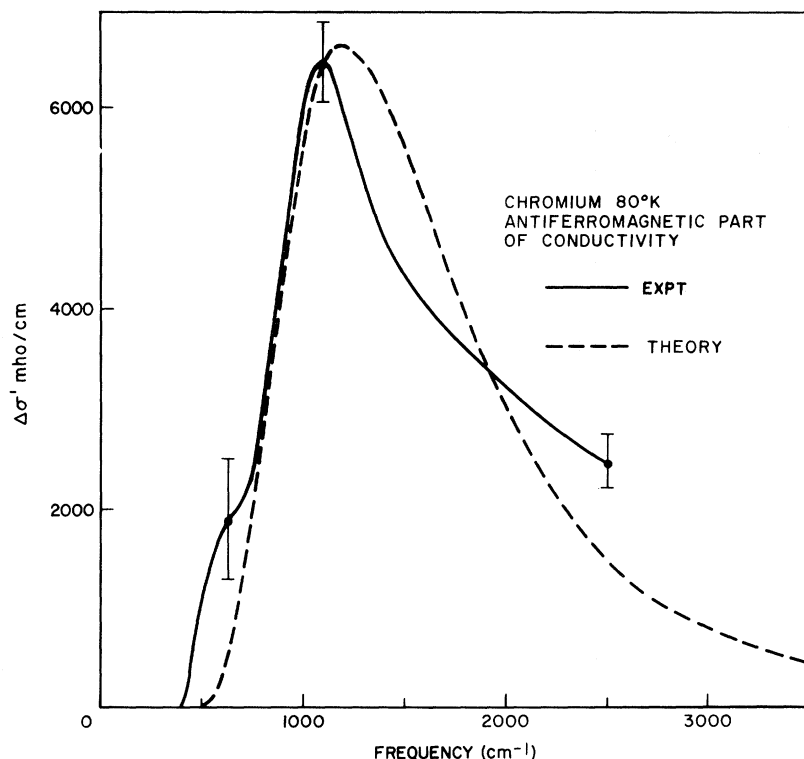


FIG. 13. Antiferromagnetic part of conductivity of chromium at 80°K compared with electron-phonon scattering theory.

E. Anisotropy

Figure 14 shows schematically the formation of domains in a chromium sample when it is cooled. It is known that domains form with \vec{Q} along various $\langle 100 \rangle$ directions of the originally cubic crystal.⁹ If a large magnetic field H_0 is present during cooling, the sample can be made single domain. The electronic properties of single domain samples are anisotropic since the electronic symmetry is tetragonal. In a single-domain sample the low-temperature dc resistivity is typically 35% higher for the measuring current \vec{I} parallel to \vec{Q} compared with the case of $\vec{I} \perp \vec{Q}$.²⁰ We picture gaps forming on pieces of Fermi surface whose velocity vectors are predominantly along \vec{Q} . The opening of these gaps for $T < T_N$ then removes more intraband conductivity for $\vec{I} \parallel \vec{Q}$. Because of weak couplings between the electrons and the lattice, the lattice parameters also show a very slight deviation from cubic symmetry. Recently, small orthorhombic and tetragonal distortions of the lattice parameters have been found for single- \vec{Q} chromium samples.²⁷ These distortions are a few parts in 10^6 and had not been detected in earlier measurements. For $T < 122^\circ\text{K}$ the sample is tetragonal with $c/a < 1$ and with the c axis along \vec{Q} .

Since energy gaps open on energy surfaces with velocity vectors principally along \vec{Q} , the infrared

absorption peak should be strongest for the infrared electric field \vec{E} parallel to \vec{Q} . Two experiments have been carried out to test this anisotropy. First a rectangular sample was prepared with $\langle 100 \rangle$ axes parallel to its edges (Fig. 14). This sample was cooled in a field of $H_0 = 25$ kOe perpendicular to one flat face. A reflectivity spectrum was measured for this face at $T = 80^\circ\text{K}$ (see E_1 in Fig. 14). Next the sample was heated above T_N and cooled with H_0 in a plane face. Spectra were then measured with the polarizations E_2 and E_3 (Fig. 14). There was no measurable difference between any of these spectra. We cannot easily abandon arguments for anisotropy because the bulk dc conductivity was found to be 10–20% higher for the E_3 geometry at 80°K . Because the f -sum integral (Table II) must be constant, the anisotropic dc conductivity must be compensated by a frequency region with reversed anisotropy in the optical conductivity. It therefore seems reasonable to postulate that at least for about the first 200 Å near the surface (the infrared skin depth), the \vec{Q} vector behaves differently than in the bulk. It is known that the \vec{Q} vector is sensitive to strain. The presence of the free surface might therefore force \vec{Q} into a special direction with respect to the surface which cannot be altered by a 25-kOe magnetic field.

A second experiment was carried out with no

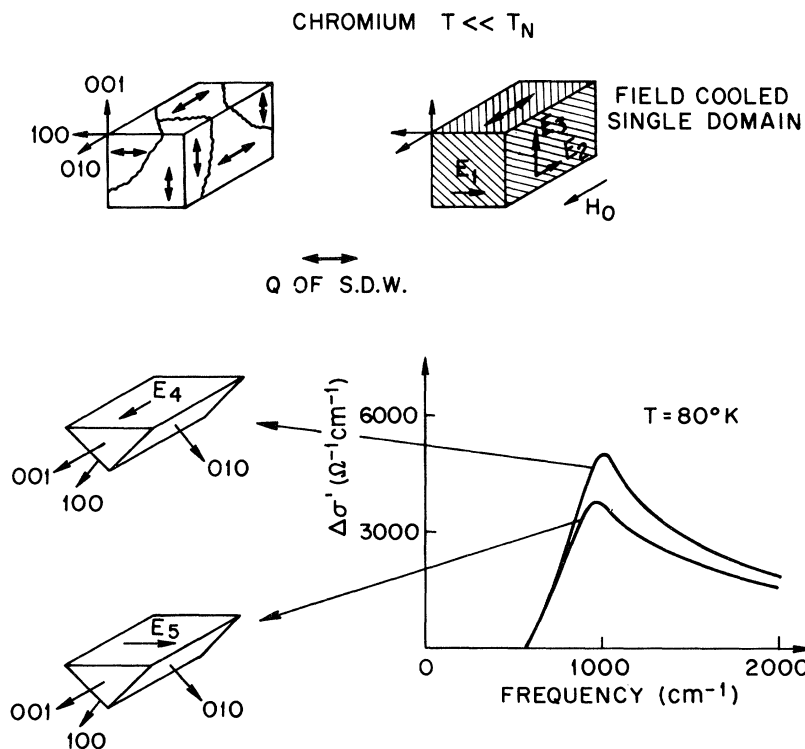


FIG. 14. Schematic picture of a polydomain and a field-cooled single-domain chromium sample. Reflectivity spectra were measured for the polarization E_1, E_2 , and E_3 . The lower part shows a polarization study of a polydomain sample for two distinct crystal faces.

magnetic field present. A sample was cut as shown in the lower part of Fig. 14 to expose a (110) face. Because of the nesting property for the bands in chromium the \vec{Q} vector must lie along a $\langle 110 \rangle$ direction. We have studied the two polarizations $\vec{E}_4 \parallel [001]$ and $\vec{E}_5 \parallel [\bar{1}10]$. A stronger absorption peak was detected for $\vec{E}_4 \parallel [001]$ (see Fig. 14). Since a cubic crystal would show identical spectra (the dielectric ellipsoid is spherical assuming normal skin effect) this confirms the anisotropic nature of chromium below T_N . The fact that the strongest absorption was found for E_4 suggests that near the surface the \vec{Q} vector is constrained to lie in the surface. Figure 14 shows that to within 10% the peaks occur at the same energy. This result serves as additional confirmation that the gap is reasonably independent of wave vector.

V. RESULTS AND DISCUSSION: CHROMIUM ALLOYS

A. Resistivity

Resistivity measurements on the alloys generally gave curves of the shape shown in Fig. 12. Often the cusp at the transition was rounded to the

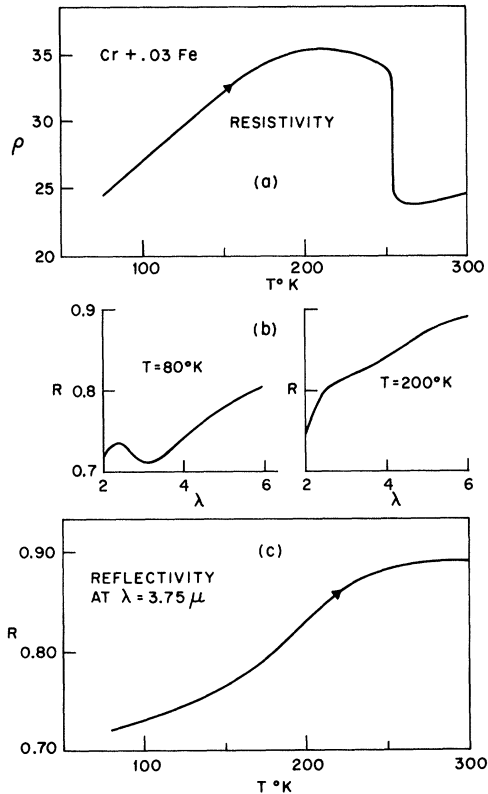


FIG. 15. (a) Resistivity of the chromium-iron alloy. (b) Reflectivity spectra near the gap energy at two temperatures. The wavelength is in microns. (c) Temperature dependence of the reflectivity near the gap energy.

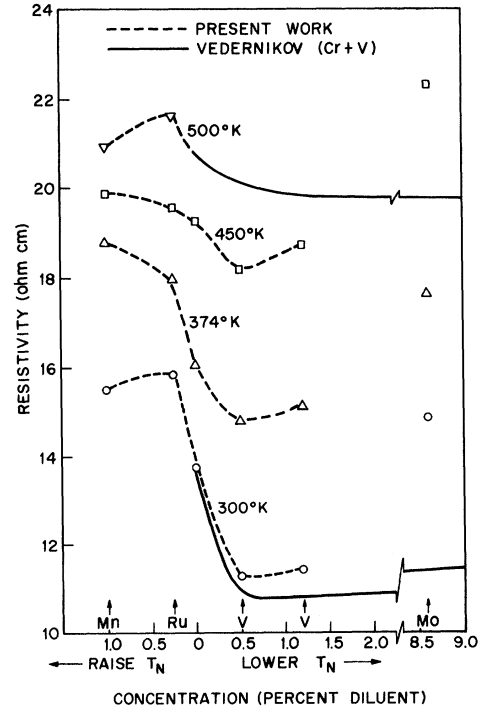


FIG. 16. Chromium alloy resistivity as a function of diluent concentration. Results for five alloys as well as pure chromium are shown by the points. Alloys to the left increase, and those to the right (except Mo) decrease the e/atom ratio. The dashed curves merely connect the experimental points.

extent of a few degrees. The temperature of this cusp is quoted as T_N in Table I. The resistivity of Cr(Fe) behaves quite differently than the other alloys.²⁸ The 3% iron sample (Fig. 15) shows an abrupt vertical jump in resistivity of 40% when cooled through 254°K. Because of the anomalous properties of Cr(Fe) we discuss it separately below.

In addition to measuring $\rho(T)$ in order to determine T_N in the alloys, some careful measurements of ρ were made at certain fixed temperatures. Vedernikov has reported on the anomalous behavior of Cr(V) resistivity.²⁹ As V is added to Cr typical alloy behavior suggests that the resistivity should rise (Matthiessen's rule). At room temperature pure Cr is already below T_N , therefore it has an increased resistance due to the presence of the gap. As V is added, T_N of the alloy is depressed below room temperature removing the gap. We expect therefore a drop in ρ with increasing V content and finally a rise as Matthiessen's rule takes over, once the gap is removed. Using this argument, we can understand qualitatively Vedernikov's result for Cr(V) at 298°K shown in Fig. 16. He finds, however, much the

same result at 500 °K where all antiferromagnetic effects should be absent. We have checked some additional alloys which lower, and some which raise, T_N to compare with Vedernikov's work. Figure 14 shows our points as well as his curves. At 374 and 450 °K for Cr(V) we confirm Vedernikov's result at low concentrations but find that ρ has recovered considerably from its minimum by the time 1.2% concentration is reached. We have also measured a Cr(Mo) alloy. Unlike V, Mo has the same valence as Cr. Mo does depress T_N , however, and pure Mo has a room-temperature resistance quite close to that of pure V. The resistance of our Cr(Mo) sample lies well above the curve for V confirming the unique behavior of Cr(V).

The behavior for alloys with more electrons than pure chromium is qualitatively quite reasonable. For the two lower temperatures shown in Fig. 16 there is a sharp rise on adding 0.25% Ru as the alloys are "more antiferromagnetic" than pure Cr and hence exhibit increased resistance due to T/T_N being smaller than for pure Cr. The points for Cr(Mn) follow a similar pattern. At the two higher temperatures they are not much higher than for pure Cr probably reflecting Matthiessen's rule.

The Cr(V) resistivity stands out as being somewhat unique though there is some ρ depression for Cr(Ti).²⁹ Vedernikov has noted the possibility of decreased s - d electron scattering causing the reduced ρ in Cr(V). We mention here another possibility – precursor effects associated with the antiferromagnetism. Figure 12 shows that in pure Cr a reasonable extrapolation of the resistance in the paramagnetic phase (dashed line) suggests extra resistance in Cr at least 25 °K above T_N . Viewed as a pure Cr effect the Cr(V) results in Fig. 16 imply an extra contribution to the resistance in pure Cr of about $2\ \Omega\ \text{cm}$ at 300 °K decreasing to $1\ \Omega\ \text{cm}$ at 500 °K. This is a large effect and it questions the validity of weak coupling models in spite of their successes in explaining other properties. Als-Nielsen and Dietrich have studied low-energy magnetic excitations (spin waves) in chromium and in a Cr(Mn) alloy.³⁰ Their neutron spectra show that the magnetic excitations change very little on raising T through T_N . These excitations were detected up to at least $T/T_N = 1.5$ confirming the presence of magnetic effects persisting far into the paramagnetic phase.

B. Low-Temperature Absorption and Energy Gap

As discussed earlier, dilute alloys of chromium with elements nearby in the atomic table are antiferromagnetic at low temperatures. Alloys have been studied (Table I) with transition temperatures

in the range 200–580 °K. Figures 17(a) and (b) show the absorption peaks associated with the transition. For each sample a small bar and a larger flat sample were prepared from adjacent slices of material. The resistivity of the bar was used to determine T_N . Samples with $T_N < 370$ °K could be measured optically above and below T_N . These samples showed absence of peaked optical structure near and above T_N as expected.

The alloys with electron-per-atom ratios less than chromium generally show broad absorption peaks at energies somewhat lower than that of pure chromium. Those with much higher electron-per-atom ratios show higher-frequency peaks which occur on the reflectivity edge near $3000\ \text{cm}^{-1}$ in some cases. Figure 18 shows this effect in $1 - R$ in detail for chromium with manganese. This figure should be compared with Fig. 6.

Figure 19 shows the frequency of the absorption peak plotted against transition temperature. As in the case of pure chromium, the peaks are broad and the best defined feature is at ω_p where the maximum in $\Delta\sigma'$ occurs. For the simplest BCS theory discussed earlier all points should lie on the line $\hbar\omega_p = 3.5kT_N$. For pure chromium the electron-phonon interaction theory gives renormalization of ω_p and T_N so that $\hbar\omega_p = 5.2kT_N$. We find that many of the low T_N alloys lie near the empirical line $\hbar\omega_p = 5.1kT_N$ which passes through the pure-chromium point. The samples with $T_N > 450$ °K give peaks well above $5.1kT_N$ up to $T_N = 550$ °K. The last two samples with the highest values of T_N show a rapid drop in peak absorption frequency. To understand and discuss the alloys further we next consider the commensurate-incommensurate transition.

C. Commensurate-Incommensurate Transition

Chromium alloys with transition temperatures well above 312 °K generally have a commensurate rather than the incommensurate (or oscillatory) SDW structure of pure chromium. Figure 19 shows that these antiferromagnets have high-energy gaps which do not scale with T_N . Three of the alloy samples [not counting Cr(Fe)] are known to exhibit both types of spin structure with a transition between them at T_{∞} (see Table I and Fig. 2). These three samples appeared to have two energy gaps in the present study; a low-energy gap for the incommensurate phase ($T < T_{\infty}$) and a higher-energy gap for $T_{\infty} < T < T_N$. Both gaps are included in Fig. 19. In each case the conductivity peaks associated with one of the gaps are quite weak; for Cr(0.003 Ru) the high-energy gap and for Cr(0.0065 Ru) the low-energy gap must be assigned with some reservation. In Cr(0.0065 Ru) particularly there is only a slight flattening in its

spectrum of R^2 near 1150 cm^{-1} for $T = 25^\circ \text{K}$ indicating a very weak absorption peak. Unlike the two other alloys, this possible low-energy gap appears while the very strong high-energy gap absorption ($\omega_p = 3200 \text{ cm}^{-1}$) remains present.

The Mn alloy exhibits both gaps most clearly. At the lower temperatures ($T = 25$ and 80°K) only the low-energy gap appears at $\omega_p = 1150 \text{ cm}^{-1}$. At 300 and 370°K only the high-energy gap is present. At 200°K , however, there is evidence of both gaps in what is nominally the commensurate phase. (We estimate $T_{co} \approx 60^\circ \text{K}$ from the known Mn concentration.) The persistence of both gaps at the same temperature was at first thought to be the result of composition fluctuations across the face of the reflecting surface. Arrott *et al.* have found $\pm 20\%$ variations in the alloy composition over distances of 50μ in their Cr(Fe) samples.¹⁴ An electron-beam microprobe experiment was done on our Cr(0.01Mn) sample. The $1\text{-}\mu$ -diam electron beam was used to excite Mn x-ray fluorescence and this signal was monitored as the beam was scanned over various parts of the sample surface. The signal was found to remain constant to $\pm 5\%$ which was the noise level. It is estimated that variations larger than $\pm 50\%$ would be needed to cause both gaps to appear at 200°K in the Mn sample. It must be noted that the rounding of the resistivity cusp at $T = T_N$ in this same sample suggests quite small composition inhomogeneities – more like the $\pm 5\%$ deduced as an upper limit from the microprobe scan. The Cr(0.003Ru) x-ray signal was too weak for meaningful microprobe scans to be made. The rounding of the resistivity cusp suggests $\pm 20\%$ composition fluctuations in this sample. Such fluctuations are too small to allow both phases to be present at 80°K . A simple interpretation, however, in terms of two spin-density waves being present simultaneously appears difficult. The energy band deformation caused by the commensurate SDW must strongly modify the smaller energy gap caused by the incommensurate SDW. This would shift the smaller gap away from $5.1kT_N$ which contradicts our data. Before leaving the alloys with two gaps, there is one additional feature to be discussed. The low-energy gap in three of the low-concentration alloys [Cr(Mn) and Cr(Ru)] is associated with an incommensurate SDW. It is important to realize that the Néel temperature listed in Table I is measured by the resistivity anomaly at high temperatures near T_N . For these alloys T_N marks the transition from the paramagnetic to the commensurate SDW state. By applying pressure (P) it is possible to force these alloys to first enter the incommensurate state on cooling. The new $T_N(P)$ may be extrapolated to $P = 0$ to obtain

the hypothetical transition temperature for the incommensurate state.³¹ In Fig. 19 we show with arrows the replotting of the gaps to correspond to this more appropriate Néel temperature. The replotted points agree reasonably well with the curve $\hbar\omega_p = 5.1kT_N$ passing through pure Cr. We conclude that for the incommensurate-antiferromagnetic state the gap (absorption peak) follows $\hbar\omega_p = 5.1kT_N$ quite well.

If we regard the values of T_N and T_{co} as anomalous in Cr(Fe) a rough pattern emerges for the alloys. We find that all of the gaps are large for commensurate alloys, with Cr(0.15Re) perhaps coming near some limiting behavior with the gap beginning to decrease with additional diluent. The gap behavior shown in Fig. 19 may be qualitatively understood as follows. At low T_N the antiferromagnetic alloys are incommensurate. In forming the antiferromagnetic phase the electron and hole pockets are coupled by a SDW of wave vector \vec{Q} such that two parts of the Fermi surface are matched or nested. \vec{Q} is slightly less than half the reciprocal-lattice vector \vec{G} . A dimensionless measure of the incommensurate wave vector is

$$\delta = (\frac{1}{2}\vec{G} - \vec{Q})a/2\pi = 1 - a\vec{Q}/2\pi. \quad (5)$$

For pure chromium $\delta = 0.05$ at low temperatures. In the incommensurate structure where there is good matching over an area A , the BCS-type theory is appropriate. Using the rigid-band model we start in pure chromium with the electron Fermi surface smaller than the hole surface. Increasing the e/atom ratio above 6.0 increases A . T_N and ω_p increase with A , and $\omega_p \propto T_N$. Near $T_N = 320^\circ \text{K}$, δ has dropped to 0.03. Further increase in e/atom ratio causes an abrupt transition to $\delta = 0$, the commensurate state. For this new state to be stable there must be an energy gap of magnitude at least

$$E_g = 0.03 \frac{2\pi}{a} \frac{\partial E}{\partial k}, \quad (6)$$

where $\partial E/\partial k$ is an average slope of the energy bands at the Fermi surfaces being matched. A rough estimate of $\partial E/\partial k^8$ gives $E_g = 2500 \text{ cm}^{-1}$, somewhat lower than the observed absorption peaks ($3500\text{--}4000 \text{ cm}^{-1}$). If we assume that the rigid-band picture continues to hold, increasing the e/atom ratio further must finally favor the incommensurate structure again. At this concentration we might expect the gap to revert to

$$\hbar\omega_p \sim 5.1kT_N.$$

Rice and Halperin have discussed the commensurate-incommensurate transition with a model consisting of spherical electron and hole pockets whose relative size can be varied. Their model can be simply visualized as an extension of the

Fedders-Martin model to include the effects of varying the e/atom ratio within the rigid-band approximation. They include a third pocket of carriers to represent the nonmagnetic part of the Fermi surface. With an equal concentration of carriers in the nonmagnetic and magnetic pockets (the case appropriate²² for Cr) when the electron pocket radius is increased, so nesting is no longer perfect, T_N drops monotonically but the gap remains constant. At a critical radius there is a first-order transition to the incommensurate state at low temperatures.¹¹ The gap drops abruptly and then both T_N and $\hbar\omega_g$ drop monotonically as the electron radius continues to increase. The results of this model are qualitatively in agreement with the main experimental results. In the commensurate phase (Fig. 19) the gap is approximately independent of transition temperature with the absorption maximum near $3500\text{--}4000\text{ cm}^{-1}$ ($\hbar\omega_p \sim 0.43\text{--}0.50\text{ eV}$). At the commensurate-incommensurate transition there is an abrupt drop in energy gap below which T_N and $\hbar\omega_p$ both decrease maintaining the ratio 5.1. The Rice-Halperin model, however, is too crude to allow a quantitative comparison with the experiments. The important experimental result is that in the commensurate phase most samples show a constant gap with maximum absorption near $3500\text{--}4000\text{ cm}^{-1}$ ($\hbar\omega_p \sim 0.43\text{--}0.50\text{ eV}$).

D. Chromium-Iron Alloys

The Cr(0.03 Fe) sample shows an anomalous 40% jump in resistivity when cooled through 254°K (Fig. 15). Similar behavior has been observed by Araj and Dunmyre.²⁸ There is a 2°K hysteresis in this jump when the sample is heated. Arrott *et al.* and Ishikawa *et al.* have studied neutron scattering for several Cr(Fe) samples.^{14, 15} Comparison with their work suggests that our samples have entered a commensurate antiferromagnetic state at 245°K . The nature of the phase just above 254°K is not clear, however, the Néel temperature may be 20°K higher though no sign of it shows up in the $\rho(T)$ curve.¹⁵ This estimate of T_N is based on the phase diagram shown in Fig. 2 and must be regarded as tentative since there is conflicting data on the phase boundaries in Cr(Fe).

The neutron diffraction studies have shown anomalous behavior for Cr(Fe) alloys.^{14, 15} The addition of iron increases the e/atom ratio and should stabilize the antiferromagnetic phase but, in reality, T_N decreases. The fact that iron possesses a local moment may explain this fact.

The Cr(Fe) alloy absorption peak occurs at 3150 cm^{-1} at 80°K . The phase diagram (Fig. 2) suggests that the sample is commensurate at this

temperature. Our observed gap energy is quite high and very similar to value to the other commensurate alloys. For the Cr(Fe) alloy we have used the temperature of the large resistivity discontinuity at 254°K as a characteristic temperature in plotting the point in Fig. 19. The point would lie closer to the other commensurate alloys if a higher T_N were used. It may be significant that a smooth extrapolation of the magnetic moment from well below 254°K to the temperature where the moment would go to zero in the absence of the transition at 254°K suggests a value for T_N well above 300°K .¹⁴

The sum-rule arguments used to discuss the strength of the absorption peak in pure Cr suggest that the abrupt and large resistivity jump in Cr(Fe) (Fig. 15) will have associated with it an abruptly appearing and strong energy gap peak ($\Delta\sigma'$) as the alloy is cooled through $T = 254^\circ\text{K}$. We have monitored the optical reflectivity at two wavelengths while heating through the transition. Figure 15 shows one such temperature scan. Contrary to expectations the reflectivity rises rather smoothly showing no abrupt behavior near 254°K . The abrupt change in dc resistivity must therefore be associated with changes in the conductivity spectrum well below our frequency range. The observed gap probably is associated with the more gradual rise in $\rho(\text{dc})$ below 254°K .

The observed Cr(Fe) absorption fits in with the conclusions of Sec. VC. The transition temperature is anomalous probably because of the local moment. The gap energy is in the range characteristic of all the commensurate alloys and must arise from the locking in of the SDW wave vector to $\frac{1}{2}G$ so that Eq. (6) is operative.

E. Discussion

Recently Bos *et al.* have measured the absorption in a series of Cr(Mn) samples.³² They measure $A = 1 - R$ directly at helium temperature. Using estimates for T_N we have added their four points to Fig. 19. These points also confirm the jump in gap at the commensurate-incommensurate transition. There are also indications of two gaps in some of their samples.³³ These authors find a gap near 4300 cm^{-1} for Cr(0.045 Mn) which is higher than any gap measured in the present study. As mentioned earlier our Ru and Re alloys with the highest transition temperatures are probably approaching some kind of limiting value for the gap energy. We note, however, that Cr(Mn) shows little sign of saturation in its T_N -versus-concentration curve even up to 6% Mn.¹²

There are two interesting questions which are associated with our optical techniques. In all optical studies of metals there is the problem of

whether the measurements are influenced by specifically surface properties. We have already discussed the anomalous-skin-effect problem. In addition there is the question of whether T_N is the same near the surface as for the bulk, and whether the \vec{Q} vector and the magnetization vector of the SDW are restricted or pinned near the surface. From the experiments (Fig. 10) an extrapolation shows that T_N of the surface is probably within 50 deg of T_N (bulk). We have already seen that the thermal smearing prevents resolution of the optical gap near T_N , so a more precise measurement of T_N (surface) cannot be extracted by our present methods.

The question of \vec{Q} near the surface has only been partially studied because of the restricted value of magnetizing field available (25 kOe). With larger fields it may be possible to shift Q perpendicular to the surface and measure the energy necessary for this shift. We do conclude that there is some pinning of Q near the surface. We have seen no effects connected with the transverse to longitudinal SDW transition. Since this transition is hardly detectable in the resistivity we can expect any associated optical effects to be weak in the infrared region. From the observation of distinct commensurate and incommensurate gaps we conclude that both states occur near the surface, however, as with the transition at T_N , the transition temperature T_{co} may be shifted from the bulk value.

Finally we should emphasize the close tolerance of the Fermi-surface nesting which is indicated by the optical-absorption peak. Band structure studies of the group-VI metals show d -band widths of about 10 eV. The gap structure we observe is sharp on this scale, being less than 0.15 eV wide for the incommensurate alloys and less than 0.4 eV wide for the commensurate alloys. This shows very close matching and probably indicates the unique situation which occurs in chromium.³⁴

ACKNOWLEDGMENTS

The authors are indebted to Dr. E. Bucher, Dr. R. M. Moon, Dr. D. N. Carlson, and Dr. F. A. Schmidt for supplying various samples used in this study. We gratefully acknowledge many helpful discussions with B. I. Halperin and T. M. Rice throughout the course of this work.

APPENDIX A: ANOMALOUS SKIN EFFECT

In this section we study the possible influence of the anomalous skin effect on the reflectivity of chromium. As mentioned in Sec. III D we use a free-electron (Drude) model for chromium to simplify the analysis. In much of the region

where the anomalous skin effect can be important in chromium, ω is greater than ω_c the collision frequency. For chromium the measured optical conductivity falls approximately as ω^{-1} rather than ω^{-2} as predicted by the Drude formula in this region:

$$\sigma = \sigma_0 / (1 + i\omega / \omega_c). \quad (\text{A1})$$

To make σ have the correct value (but not the correct slope) we choose $\omega_c = 335 \text{ cm}^{-1}$ (Table IV). We wish to check particularly possible effects near 1000 cm^{-1} where the antiferromagnetic absorption occurs. We consider two temperatures or, more precisely, two values of the collision frequency in the model; $\omega_c = 340$ and 85 cm^{-1} . The effect of this choice on σ_0 corresponds to real chromium at 300 and 120°K .

Besides the parameters σ_0 and ω_c required in the classical theory we need the Fermi velocity or some equivalent additional parameter to evaluate the anomalous skin effect. Table IV shows the parameters adopted for these test calculations. In Fig. 20 we plot $\sigma(\omega)$ for the parameters of Table IV. Also plotted are the mean free path l and the classical skin depth δ , where

$$\delta = \lambda / 4\pi k \quad (\text{A2})$$

(λ is the optical wavelength and k is the imaginary part of the index of refraction). At the higher temperature ($\omega_c = 340 \text{ cm}^{-1}$) we find $l < \delta$ over the entire frequency range and the anomalous skin-effect correction to the reflectivity is negligible. When $\omega_c = 85 \text{ cm}^{-1}$ Fig. 20 shows that $\delta < l$ over a considerable frequency range. In this range we must consider nonlocal effects.

Using the parameters in Table IV we calculate $A_0 = 1 - R_0$, the absorptivity using anomalous skin effect with diffuse reflection of electrons at the metal-air boundary. This calculation is conveniently carried out using the tables given by

TABLE IV. Free-electron model of chromium for anomalous-skin-effect study.

Parameter	Unit	Case 1	Case 2
σ_0 dc conductivity	mho/cm	0.07×10^8	0.28×10^6
ω_c collision frequency	cm^{-1}	340	85
v_F Fermi velocity	cm/sec	10^8	10^8
l mean free path	\AA	157	630
n electron density	cm^{-3}	1.58×10^{22}	1.58×10^{22}
Temperature of chromium which gives σ_0	$^\circ\text{K}$	300	120
x parameter of Table II		0.10	1.7

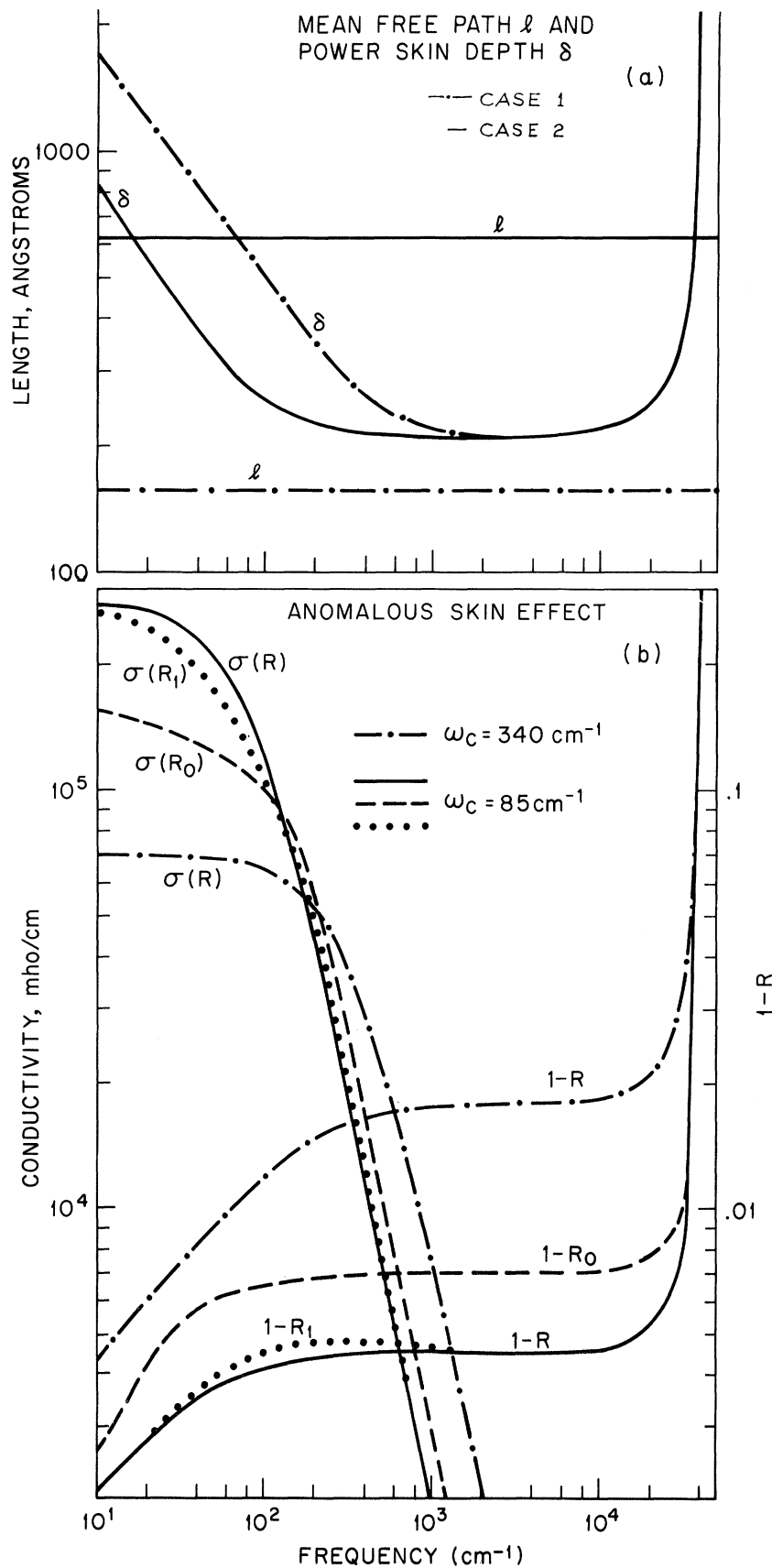


FIG. 20. (a) Mean free path and skin depth for a free-electron-gas model. All parameters are given in Table IV. For the low-collision frequency (solid curve) δ crosses ℓ giving anomalous skin effect. (b) $1-R$ for the electron gas. For $\omega_c = 85$ we show normal skin effect (R) and anomalous skin effect with diffuse (R_0) and specular (R_i) electron scattering. A Kramers-Kronig analysis has been performed on all the reflectivity curves assuming normal skin effect to obtain the conductivity curves shown.

Dingle.¹⁸ We now apply the Kramers-Kronig analysis to both R and R_0 . The analysis of the R spectrum reproduces σ [Eq. (A1)] used to calculate A , serving as a check on our method of analysis. The analysis of R_0 yields the curve labeled $\sigma'(R_0)$. This is the curve of interest. We note that $\sigma'(R_0)$ at 120 °K is different than $\sigma'(R)$ but contains no peak comparable to the antiferromagnetic peak. We take the near identity of $\sigma'(R)$ and $\sigma'(R_0)$ to justify the use of classical analysis of the reflectivity in chromium. Figure 20 shows that this procedure is good to an accuracy of about 40% in σ .

As an additional test we have also considered the case of specular surface reflection of electrons. Though it is generally believed that this case does not apply to metals, it can give more peaked structure since this type of absorption exists over a narrower frequency range. Figure 20 shows $A_1 = 1 - R_1$, the absorptivity assuming specular electron reflection. The calculations were based on the work of Reuter and Sondheimer.¹⁹ $\sigma(R_1)$ determined by Kramers-Kronig analysis of R_1 does contain a broad peak near 250 cm^{-1} which can only be resolved by plotting $\sigma'(R_1) - \sigma'(R)$. Two features rule out this type of skin effect as being responsible for the experimentally observed peak in chromium near 1000 cm^{-1} . First, the peak in $\sigma'(R_1)$ has a gradual onset of absorption; it is not abrupt like the experimentally observed absorption. Second, consideration of the temperature dependence of ω_c shows that the peak in $\sigma'(R_1)$ would decrease in frequency on cooling – opposite to the observed antiferromagnetic peak in chromium.

Returning to the A_0 anomalous skin effect, we have made additional checks such as doubling A_0 , and considering lower temperatures. The conclusion is that the anomalous skin effect cannot cause reflectivity structure that can be confused with the antiferromagnetic absorption. There may be anomalous-skin-effect absorption present in the low-temperature data; however, our classical method of analysis is adequate in reproducing the conductivity spectrum as long as we are satisfied with an uncertainty in our conductivity scale of about 40%. To fix the scale better than this would require absolute reflectivity measurements to 0.1% and better in the region below 300 cm^{-1} as well as a different method of analysis.

APPENDIX B: OPTICAL CONSTANTS OF CHROMIUM

The optical constants of chromium can be determined by a Kramers-Kronig analysis of the experimentally obtained reflectivity. This type of analysis has been presented above and is useful in showing the appearance of the antiferromagnetic peak at low temperatures. Unfortunately the anal-

ysis suffers from uncertainties due to the lack of accurate reflectivity values in the visible and ultraviolet region and also due to the sensitivity of the analysis to small changes in the input data. As a check on the Kramers-Kronig analysis a fitting procedure was also used. In this procedure a Drude term and several Lorentzian oscillator modes have their parameters adjusted to fit the reflectivity. There are two advantages to this procedure. First the modes always have a well-behaved loss characteristic which falls off in a reasonable manner outside the fitting range. This is in contrast to the Kramers-Kronig analysis which can give unphysical negative values of the loss particularly at the high-frequency limit of the data. Second, the modes can be described by a few parameters which allows an automatic least-square-fit procedure to be used. The fit proceeds by evaluating (numerically) the derivatives of the amount of misfit with respect to each parameter and then the evaluation of corrective increments. This procedure has been described in detail by others.³⁵ Various starting parameters were tried; the program always selected a Drude term plus some very broad “interband” terms giving significant conductivity in the range 100–10 000 cm^{-1} . In addition one strong “interband” term with σ' peaked near 17 000 cm^{-1} is also needed as is obvious from the data in Fig. 6.

Band-structure studies of the column 6 elements show that there are some band degeneracies along certain directions in the absence of spin-orbit coupling.⁸ In other directions in reciprocal space these bands split. The spin-orbit splitting parameter for chromium is 300 cm^{-1} . These bands can be the source therefore of low-energy interband transitions near 300 cm^{-1} . Such transitions would explain the ω^{-1} (rather than Drude ω^{-2}) frequency dependence of σ' in the range 300–3000 cm^{-1} .

Table V shows σ' for the 300 °K fit. This conductivity spectrum is noticeably larger than the Kramers-Kronig spectrum shown in Fig. 6. In the region of most interest here near 1000 cm^{-1} , the difference is 40%. Test runs using both methods of analysis show that our present reflectivity uncertainty gives a conductivity uncertainty of about 30% near 1000 cm^{-1} . A direct measurement of the optical constants with the 10.6- μ laser would obviously be useful. Two points need emphasizing here. The first is that surface preparation can cause significant reflectivity differences. We have found that even above T_N various methods of polishing and etching can cause variations in R of ± 0.005 . Thus any more careful analysis must be coupled with a surface study. Second, the position and shape of the antiferromagnetic absorption are relatively insensitive to the uncertainties described

TABLE V. Optical constants of chromium from reflectivity fits.

$\bar{\nu}$ (cm^{-1})	$\hbar\omega$ (eV)	σ' (10^4 mho/cm)	300 °K			80 °K			
			n	k	δ (Å)	σ' (10^4 mho/cm)	n	k	δ (Å)
10	0.0012	7.0	458	460	1730	35.4	695	1527	521
100	0.012	7.0	127	163	488	4.0	57	212	375
200	0.025	5.8	71	123	323	2.6	31.6	125	318
400	0.050	3.3	30.3	81.3	245	1.2	13.1	67.4	295
900	0.112	0.98	7.98	40.9	216	1.3	15.2	28.4	311
1000	0.124	0.82	6.68	37.0	215	1.5	15.4	29.3	271
1200	0.149	0.61	4.93	30.7	216	1.4	12.3	28.6	231
1500	0.186	0.43	3.56	24.0	221	0.84	6.59	25.5	208
2000	0.248	0.33	2.85	17.4	299	0.38	3.21	17.7	224
3000	0.372	0.37	3.57	10.3	257	0.36	3.59	9.94	267
5000	0.620	0.51	4.55	6.72	237	0.50	4.69	6.42	248
1.0×10^4	1.24	0.71	4.15	5.11	156	0.71	4.22	5.02	158
1.25	1.55	0.74	3.70	4.75	134	0.74	3.77	4.69	135
1.50	1.86	0.78	3.40	4.63	115	0.78	3.42	4.58	116
1.75	2.17	0.81	2.94	4.74	96	0.81	2.96	4.70	97
2.0	2.48	0.57	1.82	4.50	88	0.57	1.83	4.46	89
3.0	3.72	0.18	0.64	2.83	94	0.18	0.64	2.80	95

above. We have already included suitable strength uncertainties for the antiferromagnetic conductivity peak in an earlier section.

In Table V we list the optical constants of chromium. We use the oscillator fit procedure and list these optical constants at selected frequencies. We have carried out fits to the 80 °K chromium data using additional modes to represent the antiferromagnetic absorption. This fit is also listed in the table. Since the fitting procedure has reflectivity errors which are different in sign at the two temperatures, the Kramers-Kronig analysis

has been used to obtain the antiferromagnetic part of the conductivity. It was felt that the Kramers-Kronig method minimizes the error in the subtraction procedure used to obtain $\Delta\sigma'$. Table V gives probably more realistic values than the Kramers-Kronig method at frequencies above 3000 cm^{-1} . In this high-frequency region our values in Table V agree within the reflectivity uncertainty with the values given by Kirillova and Noskov who use an entirely different method of analysis.³⁶

¹L. Corliss, J. Hastings, and R. Weiss, Phys. Rev. Letters **3**, 211 (1959).

²G. Shirane and W. J. Takei, J. Phys. Soc. Japan Suppl. **17**, 35 (1962).

³S. A. Werner, A. Arrott, and H. Kendrick, Phys. Rev. **155**, 528 (1967).

⁴C. Herring, *Magnetism*, edited by G. T. Rado and H. Suhl (Academic, New York, 1966), Vol. 4.

⁵W. M. Lomer, Proc. Phys. Soc. (London) **80**, 489 (1962).

⁶A. W. Overhauser, Phys. Rev. **128**, 1437 (1962).

⁷P. A. Fedders and P. C. Martin, Phys. Rev. **143**, 245 (1966).

⁸L. F. Matthiess, Phys. Rev. **139**, 1893 (1965); T. L. Loucks, *ibid.* **139**, 1181 (1965).

⁹J. E. Graebner and J. A. Marcus, J. Appl. Phys. **37**, 1262 (1966).

¹⁰L. M. Falicov and D. R. Penn, Phys. Rev. **158**, 476 (1967).

¹¹T. M. Rice (unpublished).

¹²W. C. Koehler, R. M. Moon, A. L. Trego, and A. R. Mackintosh, Phys. Rev. **151**, 405 (1966).

¹³A. S. Barker, Jr., B. I. Halperin, and T. M. Rice, Phys. Rev. Letters **20**, 384 (1968); in *Proceedings of the Eleventh International Conference on Low-Temperature Physics*, edited by J. F. Allen *et al.* (University of St. Andrews Printing Department, St. Andrews, Scotland, 1969), Vol. 2.

¹⁴A. Arrott, S. A. Werner, and H. Kendrick, Phys. Rev. **153**, 624 (1967).

¹⁵Y. Ishikawa, S. Hoshino, and Y. Endoh, J. Phys. Soc. Japan **22**, 1221 (1967).

¹⁶Aluminum reflectance data is taken from H. Ehrenreich, H. R. Philipp, and B. Segall, Phys. Rev. **132**, 1918 (1963); H. E. Bennett and J. M. Bennett, *Optical Properties and Electronic Structure of Metals and Alloys* (North-Holland, Amsterdam, 1966), p. 175. Note that we obtain higher values of the conductivity than Ehrenreich *et al.* by our method of analysis.

¹⁷*American Institute of Physics Handbook*, 2nd ed. (McGraw-Hill, New York, 1957), Chap. 6.

¹⁸R. B. Dingle, Physica **19**, 311 (1953).

¹⁹G. E. H. Reuter and E. H. Sondheimer, Proc. Roy. Soc. (London) **A195**, 336 (1948).

- ²⁰A. J. Arko, J. A. Marcus, and W. A. Reed, Phys. Letters **23**, 617 (1966).
- ²¹D. B. McWhan and T. M. Rice, Phys. Rev. Letters **19**, 846 (1967).
- ²²F. Heiniger, E. Bucher, and J. Muller, Phys. Letters **19**, 163 (1965); F. Heiniger, Physik Kondensierten Materie **5**, 285 (1966).
- ²³D. W. Juenker, L. J. LeBlanc, and C. R. Martin, J. Opt. Soc. Am. **58**, 164 (1968).
- ²⁴J. C. Kimball and L. M. Falicov, Phys. Rev. Letters **20**, 1164 (1968).
- ²⁵S. H. Liu, Phys. Letters **27A**, 493 (1968).
- ²⁶T. M. Rice, A. S. Barker, Jr., B. I. Halperin, and D. B. McWhan, J. Appl. Phys. **40**, 1337 (1969).
- ²⁷M. O. Steinitz, L. W. Schwartz, J. A. Marcus, E. Fawcett, and W. A. Reed, Phys. Rev. Letters **23**, 979 (1969).
- ²⁸S. Arajs and G. R. Dunmyre, J. Appl. Phys. **37**, 1017 (1966).
- ²⁹M. V. Vedernikov, Fiz. Tverd. Tela **9**, 3018 (1967) [Soviet Phys. Solid State **9**, 2381 (1968)].
- ³⁰J. Als-Nielsen and O. W. Dietrich, Phys. Rev. Letters **22**, 290 (1969).
- ³¹A. Jayaraman, T. M. Rice, and E. Bucher, J. Appl. Phys. (to be published).
- ³²L. W. Bos, D. W. Lynch, and J. L. Stanford, Phys. Letters **30A**, 17 (1969).
- ³³J. L. Stanford (private communication).
- ³⁴T. M. Rice and B. I. Halperin, Phys. Rev. (to be published).
- ³⁵H. W. Verleur, J. Opt. Soc. Am. **58**, 1356 (1968).
- ³⁶M. M. Kirillova and M. M. Noskov, Phys. Metals Metallog. USSR **26** (1968).

Effect of Magnon Drag on Electron Mass and Mobility

Alba Theumann

Institutt for Teoretisk Fysikk, Norges Tekniske Høgskole, Trondheim, Norway

(Received 2 February 1970)

We consider an idealized model of a ferromagnetic metal where the conduction electrons of the s band interact via an exchange interaction with a system of spins represented by a Heisenberg Hamiltonian. Using double-time Green's functions, the effective mass and resistivity are evaluated to second order in the coupling of electrons to the spin system, while the spin magnetization is given by the self-consistent approximation of Bogoliubov and Tyablikov. The resistivity shows a sharp change in slope at the critical temperature that agrees qualitatively with the experimental results for gadolinium.

I. INTRODUCTION

To study the effect of magnon drag on the effective mass and transport properties of electrons in ferromagnetic metals, we consider an idealized model in which the conduction electrons of the s band interact via an exchange interaction with a system of spins of magnitude $\frac{1}{2}$ localized at the sites of a cubic lattice, and represented by a Heisenberg Hamiltonian. The model was previously considered by Methfessel and Mattis¹ in connection with the "magnetic polaron" problem.

If we represent the lattice spins by Pauli operators that commute at different sites but anticommute at the same site

$$S_i^z = b_i, \quad S_i^- = b_i^\dagger, \quad S_i^+ = \frac{1}{2}(1 - 2b_i^\dagger b_i), \quad (1)$$

$$[b_i, b_j] = [b_i, b_j^\dagger] = [b_i^\dagger, b_j^\dagger] = 0 \quad \text{if } i \neq j,$$

$$\{b_i, b_i^\dagger\} = 1, \quad (b_i)^2 = (b_i^\dagger)^2 = 0, \quad n_i = b_i^\dagger b_i, \quad (2)$$

our system is represented by a Hamiltonian

$$H = H_e + H_S + H_I, \quad (3)$$

$$H_e = \sum_{k,s} \epsilon_k a_{ks}^\dagger a_{ks}, \quad (4)$$

$$H_S = \frac{1}{2} J_0 \sum_j n_j - \frac{1}{2} \sum_{i,j} J_{ij} b_i^\dagger b_j - \frac{1}{2} \sum_{i,j} J_{ij} n_i n_j - \frac{1}{8} N J_0, \quad (5)$$

$$H_I = \frac{-g}{2N} \sum_{kk'} \sum_j e^{-i(\mathbf{k} - \mathbf{k}') \cdot \mathbf{R}_j} \{b_j^\dagger a_{k'}^\dagger a_{k,i} + b_j a_{k,i}^\dagger a_{k'}\} \\ + (\frac{1}{2} - b_j^\dagger b_j) (a_{k'}^\dagger a_{k,i} - a_{k,i}^\dagger a_{k'}). \quad (6)$$

The a_{ks}^\dagger , a_{ks} are creation and destruction operators for electrons in the conduction band with momentum \mathbf{k} , spin $s = \uparrow$ or \downarrow , and satisfy the usual anticommutation rules:

$$\{a_{ks}, a_{k's'}^\dagger\} = \delta_{kk'} \delta_{ss'}, \quad (7)$$

$$\{a_{ks}^\dagger, a_{k's'}^\dagger\} = \{a_{ks}, a_{k's'}\} = 0.$$

The square and curly brackets in Eqs. (2) and (7) mean a commutator and anticommutator, respectively. We have, in Eq. (5),

$$J_{ij} = J, \quad \text{if } i, j \text{ are nearest neighbors} \\ = 0, \quad \text{otherwise}, \quad (8)$$